



**Politecnico
di Torino**

Politecnico di Torino

Materials Engineering for Industry 4.0

Master of Science Course

July 2025

Development of Bio-based Epoxy Coatings Reinforced with Lignin for Enhanced Corrosion Protection

Tutors:

Prof. Massimo Messori

Dr. Camilla Noè

Dr. Leonardo Iannucci

Candidate:

Saba Moradi Boldaji

*To my beloved family and friends, and to the
women of my homeland, whose resilience and
strength continue to inspire my journey.*

Abstract

This study investigates the use of bio-oil reinforced with lignin as an anti-corrosion coating for mild steel. The corrosion behavior of eco-friendly, UV-curable coatings based on epoxidized soybean oil (ESO) and lignin was evaluated using electrochemical impedance spectroscopy (EIS) in a 3.5% NaCl electrolyte. The initial electrochemical impedance measurements showed that the composite coatings demonstrated superior corrosion protection, with the 3 wt.% lignin formulation reaching a peak impedance of $3.17 \times 10^8 \Omega \cdot \text{cm}^2$ within 24 hours of immersion and show a gradual reduction in low-frequency impedance modulus over time, while the unmodified ESO coatings remained below $10^4 \cdot \Omega \cdot \text{cm}^2$, which is considered a non-protective organic coating in saline environments.

Furthermore, Fourier Transform Infrared Spectroscopy (FTIR) confirmed high epoxy conversion rates in the lignin-reinforced coatings, indicating effective crosslinking during the curing process and resulting in a well-cured structure. Adhesion, pencil hardness, and solvent resistance tests on the coated samples revealed that the composite coatings exhibited excellent adhesion (5B ASTM rating) and solvent resistance as well as enhanced hardness (2H), outperforming unmodified ESO coatings.

These findings suggest that bio-polymer composites offer a sustainable alternative to non-renewable polymers in the coating industry, providing eco-friendly solutions for effective corrosion protection in industrial applications.

Table of Contents

| | |
|--|-----------|
| List of Figures..... | IV |
| List of Tables | V |
| 1. Introduction | 1 |
| 1.1. Fully Bio-based Vegetable Oil Thermoset | 2 |
| 1.2. Lignin, From Waste to Valuable Resource | 3 |
| 1.2.1. Lignin Corrosion Resistance Coatings | 4 |
| 1.3. Photopolymerization..... | 7 |
| 1.3.1. Cationic Photopolymerization | 9 |
| 1.3.2. Cationic UV Curing of Bio-based Composite Coatings | 10 |
| 1.4. Research Objective..... | 11 |
| 2. Materials and Methodology | 13 |
| 2.1. Materials..... | 13 |
| 2.2. Coating Preparation | 13 |
| 2.3. Material Characterization..... | 15 |
| 2.3.1. Viscosity and Photo-rheology | 15 |
| 2.3.2. Fourier Transform Infrared (FTIR) Spectroscopy | 16 |
| 2.3.3. Thermogravimetric Analysis (TGA)..... | 17 |
| 2.3.4. Differential Scanning Calorimetry (DSC)..... | 18 |
| 2.4. Coating Characterization | 19 |
| 2.4.1. Pencil Hardness | 19 |
| 2.4.2. Coating Adhesion..... | 20 |
| 2.4.3. Contact Angle | 21 |
| 2.4.4. Solvent Resistance Test | 21 |
| 2.4.5. Corrosion Protection Properties | 21 |
| 2.4.5.1. Electrochemical Characterizations | 21 |
| 2.4.5.2. Principle of Equivalent Electrical Circuit Modeling | 23 |
| 2.4.6. Field Emission Scanning Electron Microscopy (FE-SEM) | 25 |
| 4. Results and Discussion | 27 |

| | |
|--|----|
| 4.1. UV-Curing Process | 27 |
| 4.2. Viscosity Evaluation | 31 |
| 4.3. Photo-rheology | 32 |
| 4.4. Curing Behavior | 33 |
| 4.5. TGA | 35 |
| 4.6. Coating Hardness | 36 |
| 4.7. Contact Angle Measurement | 36 |
| 4.8. Coating Adhesion | 37 |
| 4.9. Solvent Resistance | 38 |
| 4.10. Electrochemical Impedance Spectroscopy Measurements | 38 |
| 4.10.1. Modeling of Electrochemical Impedance Spectroscopy Spectra | 41 |
| 4.11. FE-SEM Imaging | 44 |
| 5. Conclusion | 46 |
| 6. Limitations and Future Work | 47 |
| 7. References | 48 |

List of Figures

| | |
|--|-------------------------------------|
| Figure 1: Sustainable synthesis of epoxidized vegetable oils (EVOs) from Ref. 7 ⁷ | 2 |
| Figure 2: Lignin-based self-healing coatings through Diels–Alder crosslinking reactions. .. | 6 |
| Figure 3: EIS measurements of oil (ELO) with kraft lignin (LnK) ²⁶ | 7 |
| Figure 4: A Simplified Photodecomposition Process of a General Diaryliodonium Salt ³² .. | 10 |
| Figure 5: Scheme of a DSC measurement chamber | 19 |
| Figure 6: ASTM Adhesion Standards | 20 |
| Figure 7: EIS Setup..... | 22 |
| Figure 8: Electrical circuits are used to model the EIS data..... | 25 |
| Figure 9: FTIR spectra of uncured formulation containing 0%, 1%, and 3% wt. lignin..... | 28 |
| Figure 10: FTIR-T spectra before and after UV curing of ESO and ESO composites..... | 29 |
| Figure 11: FTIR-T Epoxy conversion (%) over UV exposure time with varying lignin | 30 |
| Figure 12: FTIR-T Epoxy conversion (%) over UV exposure time with varying photo initiator..... | 30 |
| Figure 13: Viscosity curve | 31 |
| Figure 14: Photo-rheology Curves..... | 33 |
| Figure 15: DSC thermograms of formulations. | 34 |
| Figure 16: TGA curves of ESO and ESO composite..... | 35 |
| Figure 17: Impedance spectra of test 2, presented as Bode diagrams, were acquired for the coatings as a function of the immersion time in the 3.5 % NaCl solution..... | 39 |
| Figure 18 : the impedance modulus ($ Z $) of L0-5-test2 at a frequency of 0.01 Hz | 40 |
| Figure 19: The impedance modulus for three coatings of test 3 at a frequency of 0.01 Hz. . | 41 |
| Figure 20: L3-5 24h and 316 h | 42 |
| Figure 21: L1-5- 24 h and 316 h..... | Error! Bookmark not defined. |
| Figure 22: L0-5- 24 h..... | Error! Bookmark not defined. |
| Figure 23: FE-SEM images of L0-5, L1-5, and L3-5 coatings after immersion | 45 |

List of Tables

| | |
|---|----|
| Table 1: Composition of the photocurable ESO formulations..... | 14 |
| Table 2: film thicknesses | 22 |
| Table 3: FTIR-ATR Epoxy conversion (%) with 5% PhI of coated films after UV curing.. | 31 |
| Table 4: Viscosity model parameters. | 32 |
| Table 5: Parameters of the photo-polymerization of ESO formulations. | 33 |
| Table 6: Glass transition temperatures in the first and second heating cycles..... | 34 |
| Table 7: TGA parameters | 35 |
| Table 8: Measurements of contact angles of coatings using water and glycerol. | 36 |
| Table 9: Results of the adhesion test for coating samples. | 37 |
| Table 10:EEC parameters computed from the EIS spectra acquired on the three coatings... | 43 |

1. Introduction

Applying coatings to surfaces is one of the most effective methods for controlling metal corrosion, which is caused by chemical and electrochemical reactions, particularly in harsh environments.¹ Metal corrosion threatens structural integrity and increases the risk of failure in construction industries (e.g., buildings, bridges), the automotive industry, and even biomedical applications involving metal-based implants. In addition to safety risks, corrosion results in significant financial losses each year. It has been reported that the estimated global cost of corrosion is approximately 5% of the world's Gross Domestic Product (GDP).²

Conventional coatings, while effective, often rely on unsustainable and environmentally unfriendly components.¹ Epoxy resins are the most commonly used coatings, renowned for their excellent chemical resistance, strong adhesive properties, and good processability. Compared to other organic polymers, cross-linked epoxies are more expensive; therefore, these high-performance materials must offer additional benefits to justify their higher cost. Moreover, the most widely used epoxy monomers are synthesized through the reaction of bis(4-hydroxyphenyl)-2,2-propane (commonly known as bisphenol A, BPA) and 1-chloropropene 2-oxide (referred to as epichlorohydrin) in the presence of sodium hydroxide. However, BPA is classified as a reprotoxic compound, capable of causing severe disruptions to the human endocrine system and posing a significant threat to wildlife. Bio-based epoxy resins offer a promising alternative to replace BPA, reducing associated health and environmental risks.³

In response to growing concerns about human health and sustainability, bio-based materials derived from natural, renewable resources have gained significant attention. Since most thermosetting polymers derived from petroleum are based on epoxy resins, and over 60% of global epoxy resin production is used in the coatings sector, thermoset bio-based polymers hold significant potential for study.⁴ These materials replace fossil-based feedstocks and provide several advantages, including non-toxicity, low-cost, high availability, and the production of materials with excellent mechanical properties.⁵ Novel coatings are being developed to address environmental challenges while ensuring superior corrosion resistance. Consequently, developing

new organic coatings with anti-corrosion properties from environmentally friendly bio-based oil has emerged as a prominent area of research.³

1.1. Fully Bio-based Vegetable Oil Thermoset

A sustainable and non-toxic alternative for epoxy production is the direct conversion of double bonds into epoxides. Due to their high double-bond content and ability to convert into multi-functional epoxides, vegetable oils serve as excellent feedstock for thermoset material production. The high unsaturation levels within the triglyceride chains of vegetable oils provide multiple reactive sites, enabling chemical modification and making them excellent precursors for multi-functionalized materials.⁶

For example, Malburet et al. explored 12 different vegetable oils, including soybean oil, linseed oil, rapeseed oil, hemp oil, safflower oil, and perilla oil. They developed a sustainable method for epoxidizing double bonds using acetic acid, hydrogen peroxide, and Amberlite®IR-120 in cyclopentyl methyl ether (CMPE). The resulting epoxidized vegetable oils (EVOs) were cured using UV and hardener-free thermal methods, and the cross-linked homopolymers exhibited enhanced thermomechanical properties in correlation with epoxy content.⁷

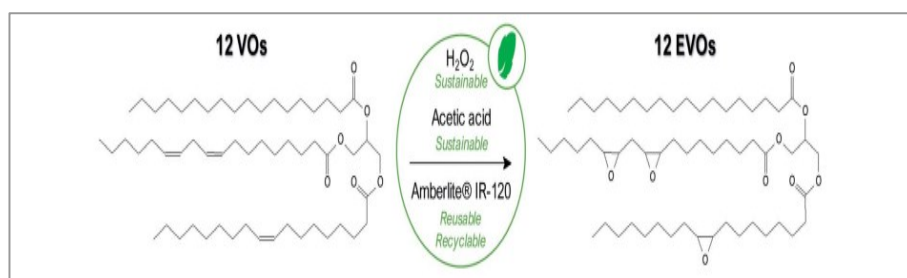


Figure 1: Sustainable synthesis of epoxidized vegetable oils (EVOs) from Ref. 7⁷

Among all vegetable oils, soybean oil, with an estimated production of 66 million tons in 2025⁸, has been widely studied in research as a bio-based polymer due to its low cost, high availability, non-depletable nature, and ability to form multi-functional epoxides.⁹

For example, Ammar et al. utilized epoxidized soybean oil to develop a fully organic multifunctional coating system with high film transparency, excellent hardness, strong adhesion, thermal stability, and effective physical barrier properties against corrosion.⁹

Epoxidized soybean oil (ESO) is synthesized in the industry by reacting with hydrogen peroxide. However, due to its flexible, long aliphatic chain, additional petroleum-based or bio-based copolymers are usually required to enhance its mechanical and thermal properties as a final structural product. Moreover, soybean oil can help achieve desired properties as a polymer matrix in bio-composites, such as increased wettability, thermal stability, and corrosion protection of organic coatings.¹⁰

Studies have been done using compounds such as gallic acid, focusing on bio-based materials.¹¹, rosin acid¹², tannic acid¹⁰, a 2,5-furan diacrylate¹³ to produce cross-linked thermoset resins, enhancing the properties of soybean oil. In addition, other green reinforcement sources, such as cellulose nanocrystals and cellulose nanofibers,¹⁴ flax fiber¹⁵, and lignin¹⁶ have been evaluated for the same purpose. However, few studies have been conducted on bio-based composites with high bio-epoxy content, highlighting the need for further research.

Due to its long hydrophobic chain, epoxidized soybean oil exhibits high flexibility and strong corrosion resistance, especially against moisture and chemicals. These properties make it a promising candidate for developing anti-corrosion bio-based epoxy coatings¹⁸. Lignin can be an ideal choice for overcoming ESO limitations. According to Zhen et al., lignin plays a crucial role in promoting the curing process of epoxidized soybean oil, significantly enhancing its strength, rigidity, and thermal properties.¹⁷ Moreover, lignin has recently been investigated as a green reinforcement in various coatings to enhance corrosion resistance in aggressive environments.¹⁸. Therefore, a deeper understanding of lignin's structure, properties, and role in bio-composites is essential for developing new sustainable materials.

1.2. Lignin, From Waste to Valuable Resource

After cellulose, lignin is the most abundant aromatic biomass resource. It originates from plant cell walls and is extensively produced as a byproduct of the pulp and paper industry and biorefineries. Based on its plant origin, lignin is typically classified into three main types: softwood

lignin, hardwood lignin, and lignin from annual plants. These types differ in the relative proportions of guaiacyl (G), syringyl (S), and 4-hydroxyphenyl (H) propane units, which are distinguished by the degree of methoxylation on their aromatic rings. Structurally, lignin consists of a complex three-dimensional polymeric network that interlinks these phenylpropane units through various chemical bonds, such as ether and carbon–carbon bonds.¹⁹ Beyond the plant source, the extraction method plays a crucial role in determining the physicochemical and thermal characteristics of lignin. The Kraft process utilizes alkaline chemicals, including sodium hydroxide and sodium sulfide, leading to Kraft lignin, which is noted for its more condensed structure and enhanced thermal stability. In contrast, the soda pulping method relies solely on sodium hydroxide, eliminating sulfur-containing agents, and generates soda lignins, usually derived from non-woody biomass sources like straw and grasses. While soda lignins lack sulfur and are considered more environmentally friendly than Kraft lignins, they tend to contain higher levels of carbohydrates and ash due to the incomplete breakdown of lignin–carbohydrate complexes during extraction. Conversely, the organosolv process employs organic solvents, such as ethanol and acid catalysts, resulting in lignin that retains a greater portion of its natural structure and functional groups. Although organosolv lignin is considered more eco-friendly and recyclable, its industrial application is not as widespread as that of Kraft lignin, which is commonly used in the pulp and paper industry.^{20,21} The presence of functional groups such as aliphatic and aromatic hydroxyl (–OH), methoxy (–OCH₃), carboxyl (–COOH), and ether bonds (C–O–C) provides lignin with the ability to form a 3D polymeric network, offering favorable physical and chemical properties such as oxidation resistance, antibacterial activity, UV resistance, water impermeability, hydrophobicity, film-forming ability, and corrosion protection.²²

Utilizing lignin to develop value-added materials, rather than limiting its use to the energy sector as fuel, not only enhances its economic value and extends its lifecycle but also offers a green alternative to petroleum-based polymers due to its unique structural and functional properties.

1.2.1. Lignin Corrosion Resistance Coatings

As a green bio-polymer, lignin is a promising candidate for use as a protective coating material due to its inherent anticorrosive properties. Due to Wang et al. Lignin's anticorrosive performance is attributed to multiple functional roles. It primarily enhances the barrier properties of coatings by

filling micropores and restricting the diffusion of corrosive agents such as water, oxygen, and chloride ions. Its complex aromatic structure and high molecular weight increase the diffusion path length, reducing the penetration of these agents to the metal surface. Additionally, functional groups in lignin, such as hydroxyl, methoxy, and carboxyl, promote strong adhesion to metal surfaces, form protective layers that adhere to surfaces, limit electrochemical activity, and enhance the long-term durability of coatings in corrosive environments. Its phenolic structure provides antioxidant activity, which helps neutralize reactive species and suppress surface oxidation. The hydrophobic character of lignin further reduces moisture absorption and slows chloride ingress.²³ In certain formulations, lignin exhibits stimulus-responsive properties. Paired with other functional materials, it enables self-healing by releasing active corrosion inhibitors upon damage, like microcracks. Due to mechanical stress or environmental factors, microcracks lead to localized pH changes or exposure of fresh metal surfaces. These conditions can initiate the breaking of lignin-inhibitor bonds or release microcapsules in the polymer matrix, allowing inhibitors to penetrate the affected area. This release counteracts corrosive agents and restores the protective layer, effectively healing the coating. Such behavior is noted in smart lignin-based polyurethanes, where inhibitors are covalently or physically attached to lignin and released upon coating disruption of the matrix.²⁴

Recent research has explored the application of lignin on different metallic substrates to assess their effectiveness as sustainable and eco-friendly protective layers. They have also explored coating preparation methods and the mechanisms responsible for performance enhancement. For example, Dastpak et al. used organosolv lignin derived from beech (hardwood) and spruce (softwood), dissolved in 1,4-dioxane, and applied it via spin coating onto stainless steel 316.² The samples were then annealed at 120 °C. The lignin coatings decreased the surface wettability, enhancing hydrophobicity and reducing susceptibility to corrosion. Corrosion behavior was evaluated using electrochemical measurements, revealing that the coatings improved corrosion resistance by up to two orders of magnitude. Among the two lignin sources, the spruce (softwood) coating showed more sustained corrosion protection after 24 hours of exposure in electrochemical impedance spectroscopy (EIS). This enhanced performance is likely due to differences in the monolignol composition, particularly the roles of syringyl and guaiacyl units and the distribution of methoxy groups in the lignin structure.

In addition, Wang et al. functionalized organosolv lignin with furan groups by reacting it with furfuryl glycidyl ether, producing a lignin-based precursor referred to as LGF. This functionalized lignin was then used to develop self-healing coatings through thermal crosslinking with 4,4'-bismaleimidodiphenylmethane (BMI). The coating solution was applied onto steel substrates using spin coating, followed by curing at 50 °C for one hour to form a uniform polymeric film, as illustrated in Figure 2.²⁵ The prepared coating demonstrates self-healing ability through thermal treatment using the reversible Diels–Alder (DA) crosslinking strategy. Specifically, the DA bonds dissociate at elevated temperature (120 °C) and reform upon cooling to 60 °C, enabling damage recovery in the polymer network. Moreover, potentiodynamic polarization (PDP) measurements showed that the corrosion rate was reduced by over 3500 times in the coated sample compared to bare steel. This significant improvement is attributed to forming a smooth, compact surface layer without plasticizers, effectively hindering the penetration of moisture and oxygen to the underlying metal.

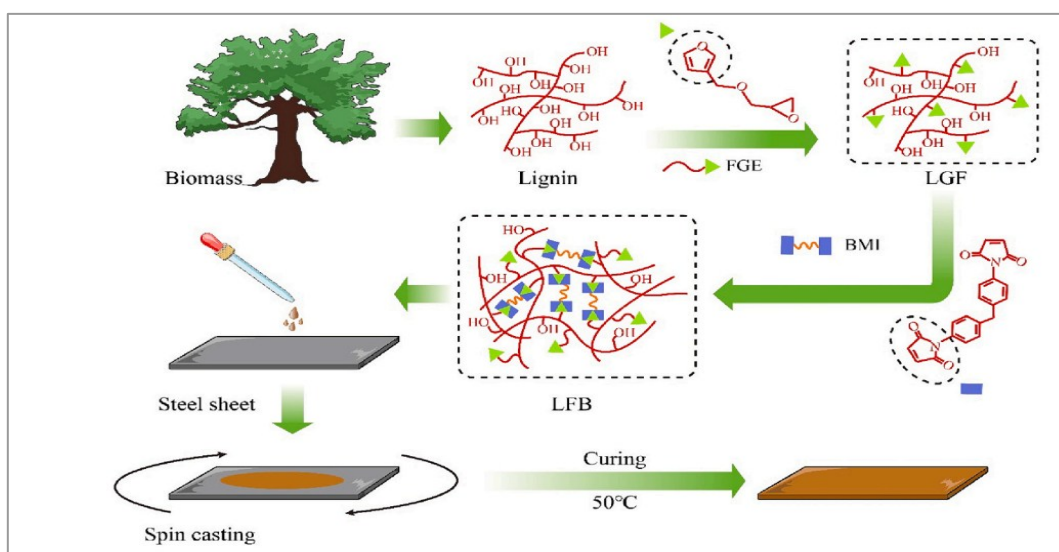


Figure 2: Fabrication of lignin-based self-healing coatings through Diels–Alder crosslinking reactions.

Regarding sustainable composite coatings, Komartin et al. developed green coatings by using epoxidized linseed oil (ELO) with kraft lignin (LnK) in varying concentrations (S1=5%, S2=10%, and S3=15%) and applying them to carbon steel surfaces.²⁶ The curing process involved two stages: an initial UV irradiation for 15 minutes ($\lambda = 365$ nm, power 8 W) and thermal treatment at 80 °C for 23 hours. The findings revealed that lignin content significantly affected thermal stability, particularly in oxidative environments. As the lignin percentage increased, thermal stability

decreased, with the 5% LnK sample showing the highest resistance to thermal degradation in air. On the other hand, higher lignin content enhanced the mechanical performance of the coatings, likely due to the reinforcing effect of lignin's rigid aromatic unit. Also, as shown in Figure 3, electrochemical measurements confirmed a significant increase in corrosion inhibition efficiency (IE), ranging from 140% to 380%, with the best performance observed in the 5% LnK coating, highlighting the promising potential of these bio-based composites for corrosion protection.

| Sample Code | A * | | | | B * | | | |
|-------------|-----------------------------|------------------------------|---------------------------|--------|-----------------------------|------------------------------|---------------------------|--------|
| | R1 (ohm * cm ²) | R2 (kohm * cm ²) | Cdl (pF/cm ²) | IE (%) | R1 (ohm * cm ²) | R2 (kohm * cm ²) | Cdl (pF/cm ²) | IE (%) |
| OL | 111.80 | 6.48 | 43.69 10 ⁶ | - | 45.83 | 37.50 | 84.87 10 ⁶ | - |
| Sr | 63.83 | 41.43 | 307.30 | 84.35 | 38.52 | 49.53 | 321.20 | 24.29 |
| S1 | 92.99 | 20,600.00 | 691.90 | 99.97 | 41.63 | 17,350.00 | 366.80 | 99.78 |
| S2 | 132.00 | 405.90 | 43.90 | 98.40 | 224.00 | 596.30 | 53.37 | 93.71 |
| S3 | 70.04 | 390.40 | 290.10 | 98.34 | 40.90 | 501.70 | 225.80 | 92.53 |

A: after 30 min immersion in the 3.5% NaCl solution; B: after the accelerated corrosion test in the 3.5% NaCl solution.

Figure 3: Electrochemical parameters obtained from EIS measurements of oil (ELO) with kraft lignin (LnK) ²⁶

Although previous studies have demonstrated the potential of lignin-based coatings for enhancing corrosion resistance, developing lignin-based bio-thermosets still faces specific challenges, particularly when incorporating different bio-derived components. As discussed earlier, soybean oil has shown promising anticorrosion properties, and adding lignin as a reinforcing agent not only helps address existing limitations but may also contribute to improved corrosion protection. In this context, Zhou et al. developed fully bio-based thermosets using multicarboxylated lignin (MGL), epoxidized soybean oil (ESO), and citric acid (CA), aiming to achieve a balance of rigidity, flexibility, and degradability. ¹⁶ The formulations included lignin at concentrations of 10%, 20%, and 30% by weight, and the results showed that increasing lignin content led to notable improvements in mechanical strength and thermal stability, mainly due to its rigid aromatic structure and its contribution to higher crosslink density. The best mechanical performance was observed in samples with better lignin content. However, the study did not examine the corrosion resistance of these composites, leaving a gap in evaluating their full potential for protective coating applications.

1.3. Photopolymerization

Thermal curing has traditionally been the conventional method for chemically crosslink thermosetting polymer composites, relying on heat to initiate and promote crosslinking within the

resin matrix, such as infrared heating, laser application, microwave energy, hot shoe methods, hot gas processes, flame treatment, oven heating, induction heating, ultrasonic methods, and resistance heating.²⁷ Each technique offers advantages and is selected based on the application's requirements. However, a significant limitation of thermal curing lies in polymeric resins' inherently low thermal conductivity, which leads to reduced curing efficiency. This issue is critical in thicker composites, where uneven thermal energy distribution results in slow heat transfer and elevated energy consumption. Non-uniform temperature profiles can also cause uneven curing and generate residual stresses that compromise the final product's mechanical properties and structural integrity. Additionally, gradual heating rates of approximately 1–2°C per minute are often employed to avoid thermal degradation, further prolonging the curing cycle and increasing energy costs.²⁸

Extensive research has been undertaken to identify alternative cross-linking methods to address these challenges. Radiation curing, particularly ultraviolet (UV), has gained attention as an environmentally friendly solution. UV curing is an advanced polymerization technique that employs ultraviolet light to initiate the crosslinking reaction of polymers. In contrast to thermal curing, which relies on conductive heat transfer, UV curing utilizes the absorption of UV radiation by photo-initiators in the resin formulation. This distinction highlights the unique benefits of UV curing across different applications. This method is characterized by rapid execution, often occurring at ambient temperatures and within a short cycle. Although bio-based thermosetting materials are environmentally friendly, many have limitations related to their processability with thermal curing, such as long and high curing temperatures. Moreover, most curing processes involve the release of volatile organic compounds (VOCs). To avoid these problems, UV-curing technology is gaining increasing attention to enhance safety and working conditions while boosting curing processes. This method is often considered environmentally friendly due to its lower air pollution by low VOC emissions.²⁹

Photo-initiators play a crucial role in facilitating the curing reaction in UV-curable systems *via* chain-growth mechanism. They determine whether polymerization occurs through a radical or cationic process. Cationic UV curing is a specific type of reaction that has gained significant interest, particularly for epoxy-based and vinyl ether monomers.

1.3.1. Cationic Photopolymerization

Cationic UV curing offers several benefits over free-radical photopolymerization. One significant advantage is that the curing process remains largely unaffected by oxygen, often negating the requirement for an inert atmosphere. Polymerization can persist even after the UV light source is turned off, potentially resulting in higher monomer conversion at room temperature or during subsequent thermal treatment. Cationic photocurable monomers are also generally linked to reduced toxicity and irritancy compared to the radical photopolymerization reaction. Furthermore, the final materials usually exhibit shrinkage upon curing and better thermal stability.³⁰

Crivello in 1977 discovered that certain diaryliodonium salts generate strong Brønsted acids when exposed to UV light. Onium salts, especially diaryl iodonium and triaryl sulfonium salts, play a crucial role in cationic photopolymerization initiation due to their reactivity and excellent solubility in non-polar monomers. Extensive studies have been conducted on these salts in both academic and industrial fields for various types of monomer polymerization. Other cationic photo-initiators include pyridinium, phosphonium, bismuthium, anilinium, and pyrylium salts, which operate through mechanisms such as direct light photolysis, free-radical promoted cationic photopolymerization, and photosensitized reactions activated by UV-visible light exposure. However, aspects like the spectral sensitivity of onium salts and the limited penetration depth of UV light can hinder the efficiency of cationic photopolymerization. This limitation influences the thickness of processable layers, requiring consideration.³¹

Onium salts are ionic compounds composed of an organic cation and an inorganic anion. The typical wavelength range for UV activation of these photo-initiators is 230 to 300 nm. The cationic part absorbs light, affecting factors such as photosensitivity, quantum yield, and thermal stability of the salt. In contrast, the anionic portion determines the strength of the acid produced, the efficiency of the initiator, and how the ion pairs react during the polymerization process. Figure 4 illustrates the simplified photodecomposition of general diaryliodonium salts. Breaking the Ar-I bond results in the formation of reactive cations, radical cations, and radicals. These entities subsequently react with proton donor species, such as solvents or monomers, to produce Brønsted acids, which act as the main initiators. The photolysis of these salts is irreversible, and the resulting acids are known as superacids. An increase in anionic size leads to a decrease in nucleophilicity,

producing stronger acids upon photogeneration. Thus, while anions do not directly influence photochemistry, their structural characteristics significantly impact the polymerization.³²

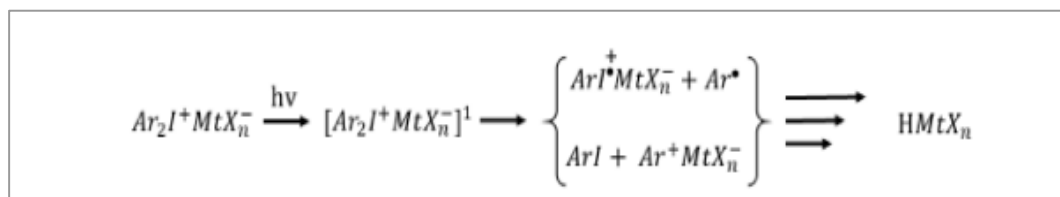


Figure 4: A Simplified Photodecomposition Process of a General Diaryliodonium Salt ³²

1.3.2. Cationic UV Curing of Bio-based Composite Coatings

Cationic UV curing facilitates the development of bio-based composite coatings by enabling rapid, solvent-free film formation and effective crosslinking, resulting in networks that exhibit strong adhesion, chemical resistance, and durability, which are vital for protection surfaces. The final coatings' performance can be tailored by modifying the chemical structure of the bio-based monomers, leading to a diverse range of thermo-mechanical properties suited for specific applications.³³ Moreover, the integration of renewable resources, especially vegetable oils, as essential components is gaining more popularity. Various studies have investigated the combination of bio-based monomers, such as palm oil and starch copolymers, with synthetic materials for coatings using cationic photo-initiators^{34,35} While others focus on completely bio-based composites.

Recent research indicates that coatings are becoming a vital application for the photopolymerization of biopolymers. Previously mentioned, Komartin et al. investigated composite materials made from epoxidized linseed oil (ELO) and kraft lignin (LnK), using triarylsulfonium hexafluoroantimonate as the UV photo-initiator in a two-step curing process involving thermal treatment.²⁶

Pezzana et al. have developed bio-based systems that utilize epoxy resin made from isosorbide, reinforced with macadamia nutshell powder. They employed a curing method based on UV cationic polymerization, using triarylsulfonium hexafluoroantimonate salt as a photo-initiator. This research highlighted the efficacy of cationic photopolymerization in bio-material

applications, particularly in achieving high conversion rates and enhancing mechanical properties. Adding macadamia shell powder considerably improved the coatings' hardness and thermal characteristics, showcasing the feasibility of using agricultural waste fillers in UV-curable bio-epoxy systems to produce durable coatings.³⁶

Furthermore, Noè et al. developed environmentally friendly anticorrosion coatings utilizing a vanillin-derived epoxy resin (DGEVA) reinforced with nano clay and applied to mild steel substrates. The formulations underwent curing through cationic UV photopolymerization, with a triarylsulfonium salt as the photo-initiator, followed by mild thermal post-treatment to enhance epoxy conversion. Incorporating nano clay improved the dispersion and mechanical strength of the coatings, thereby significantly augmenting their barrier properties. Electrochemical impedance spectroscopy indicated a robust anticorrosion performance, with the coatings maintaining elevated impedance moduli even after prolonged immersion in a 3.5% NaCl solution. Introducing nano clay further increased the coating's resistance and diminished corrosion kinetics by prolonging the diffusion path for corrosive ions.³⁷ These results emphasize the promise of bio-based photocurable composites as sustainable alternatives to traditional coatings for corrosion protection on metal surfaces.

1.4. Research Objective

While the advantages of lignin as a corrosion-resistant coating are well established, its potential as a bio-based filler has not been fully explored for developing composite and reinforced polymer materials. This strategy fosters the advancement of sustainable materials and reduces reliance on conventional inorganic fillers. Importantly, using physically mixed lignin rather than chemically grafted alternatives is beneficial because it facilitates the production of entirely bio-based composites, ensuring simplicity, cost-effectiveness, and structural integrity. Moreover, cationic UV curing has proven to be an efficient technique for processing bio-based epoxy resins, enabling energy-saving curing processes and minimizing dependence on fossil-derived materials. Various epoxy systems, including those from vegetable oils, have been studied to meet performance and application requirements. However, to our knowledge, research has yet to investigate the cationic UV curing of blends that combine epoxidized soybean oil with lignin, indicating a promising path for future exploration in sustainable coatings.

This study seeks to accomplish the following key objectives:

1. Investigate the corrosion resistance of coatings created by physically mixing epoxidized soybean oil and lignin.
2. Study the lignin content and coating formulation to ensure durable corrosion protection for metal substrates.
3. Perform a comprehensive material characterization to evaluate the impact of lignin on the thermal, mechanical, and barrier properties of vegetable oil-based thermoset coatings.

2. Materials and Methodology

This section describes the employed materials, the coating design, characterization, and corrosion evaluation. It also introduces the monitoring methods for coating corrosion conditions.

2.1. Materials

The epoxidized soybean oil (ESO) used in this study, ESBO, was provided by Cargill Bioindustrial and used without further modification. Commercial technical soda lignin Protobind® 1000, derived from Sarkanda grass and obtained from GreenValue Enterprises LLC, as a bio-based filler. This lignin was supplied as a dry powder, with a solids content ranging from 97.5% to 98.6% and a pH of approximately 3.5 in a 10% aqueous dispersion. Triarylsulfonium hexafluorophosphate salt, mixed at 50 wt% in propylene carbonate, was purchased from Sigma-Aldrich. A mild steel substrate with a composition of 0.10 wt% C, 0.60 wt% Mn, 0.20 wt% Ni, 0.15 wt% Cr, and balanced Fe is used.

2.2. Coating Preparation

To create the coating, ESO was initially heated to 40 °C to attain a fully liquid state. Various concentrations of lignin were added, as shown in Table 1. Before mixing, the lignin was dried in an oven at 60 °C for 24 hours to remove excess moisture. The ESO and lignin mixture was stirred using an IKA ULTRA-TURRAX® digital disperser to ensure a uniform lignin dispersion. This blend was homogenized at 20,000 rpm for 5 minutes. Following this, triarylsulfonium hexafluorophosphate salt was added as the cationic photoinitiator, detailed in Table 1 for each formulation. The mixture underwent an additional 10 minutes of homogenization under the same conditions. To further improve dispersion uniformity, the formulation was sonicated for 15 minutes.

Table 1: Composition of the photocurable ESO formulations.

| Formulations | ESO [%wt] | Lignin [%wt] | TAS-PF ₆ (phr) |
|--------------|-----------|--------------|---------------------------|
| L0-3 | 100 | 0 | 3 |
| L0-5 | | | 5 |
| L0-9 | | | 9 |
| L0-11 | | | 11 |
| L1-3 | 99 | 1 | 3 |
| L1-5 | | | 5 |
| L1-9 | | | 9 |
| L1-11 | | | 11 |
| L3-3 | 97 | 3 | 3 |
| L3-5 | | | 5 |
| L3-9 | | | 9 |
| L3-11 | | | 11 |

The steel substrates were polished with silicon carbide abrasive paper up to 800 grit to ensure optimal coating adhesion. Using a spiral bar coater, the formulation containing ESO, a photo-initiator, and lignin was applied on steel substrates. The film underwent crosslinking under a Dymax ECE 5000 Flood lamp for 4 minutes, exposed to UV light with an intensity of 35 mW/cm². The thickness of the cured coatings was measured using a digital thickness gauge (Mitutoyo Absolute Digimatic, Japan), achieving a measurement resolution of 0.001 mm to provide an accurate thickness for each sample.

2.3. Material Characterization

2.3.1. Viscosity and Photo-rheology

Viscosity measurements were carried out using the Anton Paar MCR 302(Graz, Austria) rheometer with a parallel plate geometry. The setup consisted of two flat plates with a gap of 300 μm , and measurements were conducted at a controlled temperature of 25 $^{\circ}\text{C}$. Viscosity was recorded as a function of shear rate ($\dot{\gamma}$), ranging from 100 s^{-1} to 0.1 s^{-1} .

The rheological behavior of the tested formulation can be characterized using the power law model (two-term model, Equation (1)) and the Sisko model (three-term model, Equation (2)).⁴

$$\eta = K\dot{\gamma}^{n-1} \quad \text{Equation 1}$$

$$\eta = \eta_{\infty} + K\dot{\gamma}^{n-1} \quad \text{Equation 2}$$

η denotes viscosity, $\dot{\gamma}$ signifies the shear rate, K indicates the consistency index, n refers to the flow behavior index, and η_{∞} represents viscosity at infinite shear rate.

Photo-rheology is a sophisticated method for evaluating the curing kinetics of materials when exposed to light. In this process, a sample is situated between two parallel plates and is subjected to oscillatory shear stress or strain. This setup enables measuring the storage modulus (G') and loss modulus (G'') upon curing. The method involves the incorporation of a light source, typically ultraviolet (UV) or visible light, that irradiates the sample during the testing phase and monitors the photocuring kinetics. In a time-sweep experiment, continuous light exposure occurs as the rheometer measures the viscoelastic response. At first, the material is a low-viscosity liquid. The polymer network forms upon light exposure, typically signaled by increased storage modulus (G'). When G' exceeds G'' , this point is known as the gel point, indicating a transition from liquid to solid-like behavior.

Photo-rheology experiments were conducted using the same instrument, an Anton Paar Modular Compact Rheometer equipped with a parallel plate configuration ($\varnothing = 25 \text{ mm}$) and a quartz bottom plate to allow UV light transmission. The gap was fixed at 300 μm , and all measurements were performed at 25 $^{\circ}\text{C}$. Time sweep tests were conducted in the linear viscoelastic region (LVR) under a constant strain amplitude of 0.5% and an angular frequency of 6 rad/s. UV

irradiation was initiated after 30 seconds using a UV Hamamatsu LC8 lamp (Hamamatsu City, Japan) at an intensity of 32 mW/cm^2 , with light exposure from the bottom. The evolution of G' and G'' was monitored over time to assess crosslinking kinetics and the final mechanical performance of the cured material.

2.3.2. Fourier Transform Infrared (FTIR) Spectroscopy

Fourier Transform Infrared (FTIR) spectroscopy is a widely used non-destructive analytical method for identifying chemical bonds and functional groups in materials by analyzing their infrared (IR) radiation absorption. This technique provides essential insights into materials' molecular structure and composition, allowing researchers to connect particular chemical characteristics to material properties or verify the effects of chemical modifications like cross-linking, grafting, or functionalization.

FTIR spectroscopy passes a broad IR radiation spectrum through the sample. Molecular bonds within the material absorb specific IR light frequencies, corresponding to the energy necessary for their vibrational transitions. Each type of chemical bond shows distinct vibrational frequencies, absorbing IR radiation at unique wavenumbers determined by bond strength and atomic masses of the linked atoms.

FTIR spectrometers utilize a Michelson interferometer to modulate the IR beam and produce an interferogram, a time-domain signal that encapsulates all spectral information. This signal is mathematically transformed into a frequency-domain spectrum using a Fourier Transform, yielding an IR absorption spectrum that acts as the sample's molecular fingerprint.

FTIR measurements can be conducted in various modes based on the sample type and analytical requirements:

- Transmission mode, where IR light travels through a thin sample or film.
- Reflection modes include specular reflection for smooth surfaces and diffuse reflection (DRIFTS) for powders and rough surfaces.
- Attenuated Total Reflection (ATR) mode is a widely used technique today. In this mode, IR light reflects internally within a crystal in contact with the sample. An evanescent wave probes only a shallow layer (typically 1–5 micrometers) of the sample. ATR simplifies

sample preparation and is particularly advantageous for analyzing solids, liquids, gels, and biological materials without extensive preparation.

The resulting spectrum displays characteristic absorption bands that can be correlated with standard reference data to ascertain the functional groups present in the material. An Infrared Absorption Table (or FTIR correlation chart) frequently matches detected peaks with specific bond types and vibrational modes (e.g., –OH stretching, C=O stretching, N–H bending). These reference tables are especially invaluable for analyzing complex spectra, particularly in systems involving polymers, composites, or chemically modified surfaces.³⁸

This study obtained FTIR spectra using a Nicolet iS50 Spectrometer in transmission mode. Measurements were performed on all formulations listed in Table 1 to optimize the photo-initiator. The wavenumber range for the measurements was 500–4000 cm^{-1} starting with uncured samples, followed by collecting spectra at different UV-irradiation time steps using a static DYMAX lamp at 0, 10, 20, 30, 40, 50, 60, 120, 180, and 240 seconds. All spectra were collected in air, with a scanning speed of one scan every 1.2 seconds and a spectral resolution of 4.0 cm^{-1} to confirm the results, FTIR measurements of the optimal PhI formulation were also conducted in ATR mode before curing and post-curing on the metal substrate, before corrosion testing. Spectra were recorded and processed using Thermo Scientific OMNIC Spectra Software, with each measurement repeated in duplicate to ensure reliable reproducibility.

The conversion of epoxy groups was assessed by tracking the reduction in intensity of the absorption peak at 840 cm^{-1} , which is specific to the epoxy functional group. The conversion percentage was determined using the following formula:

$$Conversion (\%) = (1 - (A_{post} / A_{pre})) \times 100 \quad \text{Equation 3}$$

- A_{pre} : Peak area of the epoxy group before curing
- A_{post} : Peak area of the epoxy group after curing

2.3.3. Thermogravimetric Analysis (TGA)

Thermogravimetric Analysis (TGA) is a technique for thermal characterization that tracks a material's mass during a controlled temperature increase. The main goal of TGA is to assess a substance's thermal stability and composition by measuring weight changes as it heats up. In a

typical TGA test, a small sample, often a dried film or fragment, is placed on a high-sensitivity microbalance within a programmable furnace. The sample is then heated at a constant rate (e.g., 10 °C/min), either in an inert gas atmosphere (like nitrogen or argon) or in air, depending on the needs of the analysis. As the temperature increases, the system continuously records the sample's mass changes, generating a thermogravimetric (TGA) curve that highlights important thermal parameters, including:

(1) The onset temperature of degradation indicates the point at which significant mass loss begins and thus defines the material's thermal stability threshold.

(2) The temperature corresponding to the maximum rate of weight loss, determined by the first derivative of the TGA curve (DTG), which is typically presented as a peak and helps compare the degradation profiles of different materials or identify multi-step decomposition processes.

(3) The residual mass at high temperatures provides insight into inorganic content or char formation.

In this experiment, TGA was conducted using a Mettler Toledo TGA/SDTA 851e to assess the thermal stability of the films obtained. Samples weighing 10–12 mg were placed in alumina cups and heated at a rate of 10 °C from 25 °C to 800 °C under air flow.

2.3.4. Differential Scanning Calorimetry (DSC)

Differential Scanning Calorimetry (DSC) is a thermo-analytical technique commonly used to study how materials respond to temperature changes. The analysis occurs within a specialized chamber that measures the difference in heat flow between a test sample and a reference crucible, the latter having a constant heat capacity throughout the experiment. As temperature rises at a controlled linear rate, the material may undergo various physical transitions, such as the glass transition, crystallization, or melting, depending on its thermal characteristics.

To identify these transitions, the instrument keeps both the sample and the reference at the same temperature while monitoring variations in heat flow. The collected data are presented in a thermogram, with temperature plotted on the x-axis and heat flow on the y-axis. This graph is then analyzed to determine the enthalpies of transitions.

Figure 5 illustrates the layout of a typical DSC measurement chamber. Crucibles used in DSC analysis can be made from aluminum, copper, gold, alumina, or platinum, depending on the sample's nature. Most crucibles are designed with perforated lids to allow the entry of a controlled atmosphere during measurement.

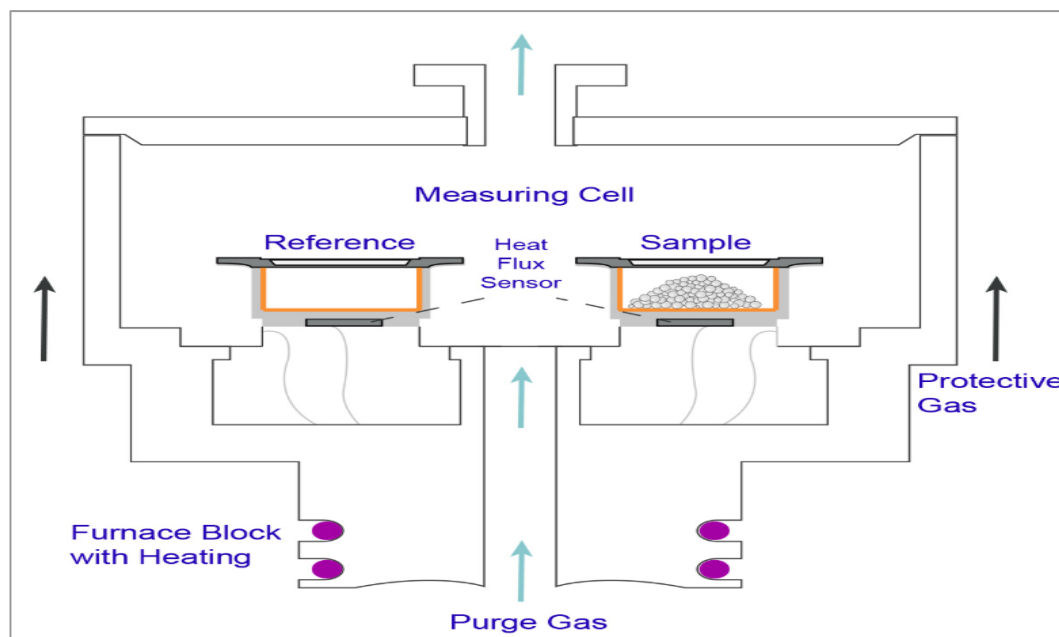


Figure 5: Scheme of a DSC measurement chamber

DSC was used in this study to evaluate the thermal transitions of the ESO–lignin composites in comparison to the pristine ESO sample. Measurements were conducted using a DSC 214 Polyma instrument (NETZSCH-Gerätebau GmbH, Germany) at a heating rate of 10 °C/min, employing 100 μ L aluminum crucibles under an Argon atmosphere.

2.4. Coating Characterization

2.4.1. Pencil Hardness

The pencil hardness test was conducted by ASTM D3363–74, using pencils to decrease hardness starting from 6H. Each pencil was held at a 45° angle and drawn across the coated surface over a distance of at least 6 mm, applying uniform pressure and speed. The coating's hardness was determined by identifying the hardest pencil that produced a scratch no longer than 3 mm inside the 6 mm stroke, indicating limited surface damage.

2.4.2. Coating Adhesion

Coating adhesion was evaluated according to ASTM D3359-B. A cross-hatch pattern was made on the coated surface using a cutting blade with six teeth spaced apart by 2 mm, resulting in intersecting vertical and horizontal cuts. Adhesive tape was applied firmly over the grid and removed at a 180° angle. The adhesion rating was determined by the percentage of undamaged squares after tape removal. The cross-hatched test area was visually compared to ASTM standards, as depicted in Figure 6.

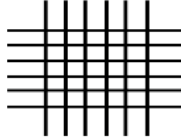
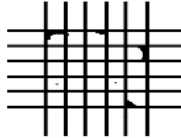
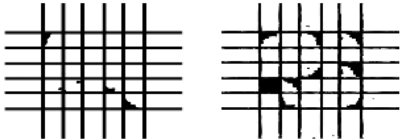
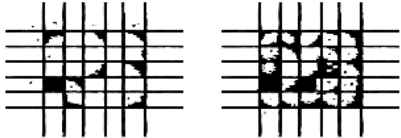
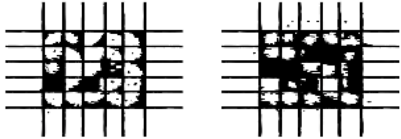
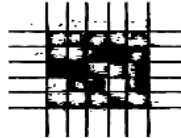
| | |
|--|--|
| ISO Class: 0/ASTM Class: 5B The edges of the cuts are completely smooth; none of the squares of the lattice is detached |  |
| ISO Class: 1/ASTM Class: 4B Detachment of small flakes of the coating at the intersections of the cuts. A cross-cut area not significantly greater than 5% is affected. |  |
| ISO Class: 2/ASTM Class: 3B The coating has flaked along the edges and/or at the intersections of the cuts. A cross-cut area significantly greater than 5%, but not significantly greater than 15% is affected. |  |
| ISO Class: 3/ASTM Class: 2B The coating has flaked along the edges of the cuts partly or wholly in large ribbons, and/or it has flaked partly or wholly on different parts of the squares. A cross-cut area significantly greater than 15%, but not significantly greater than 35%, is affected. |  |
| ISO Class: 4/ASTM Class: 1B The coating has flaked along the edges of the cuts in large ribbons, and/or some squares have detached partly or wholly. A cross-cut area significantly greater than 35%, but not significantly greater than 65% is affected. |  |
| ISO Class: 5/ASTM Class: 0B Any degree of flaking that cannot even be classified by classification 4. |  |

Figure 6: ASTM Adhesion Standards

2.4.3. Contact Angle

Contact angle measurements were carried out using an OCA 20 goniometer (Dataphysics Co., Germany), equipped with a high-resolution CCD camera and a 500 μ L Hamilton syringe. At room temperature, droplets of testing liquids, distilled water and glycerol, were deposited on the coating surfaces using the sessile drop method. The system recorded sequential images at a capture rate of 30.02 frames per second. Each contact angle was computed using integrated image analysis software, and the measurements were repeated twice for reproducibility.

2.4.4. Solvent Resistance Test

Solvent resistance was evaluated according to the ASTM D5402 standard solvent rub method. A cotton cloth, soaked in toluene, was applied to the coated surface with moderate pressure (approximately 1000–2000 g), and the cloth remained saturated throughout the duration of the test. The test area, measuring 100×25 mm, was rubbed back and forth, with each forward-and-back motion counted as one double rub. Rubbing continued until metal surfaces were observed.

2.4.5. Corrosion Protection Properties

The corrosion resistance of the coated samples was assessed using electrochemical impedance spectroscopy (EIS), one of the most effective non-destructive techniques for evaluating materials' electrochemical behavior. This method examines the impedance magnitude and phase over different frequencies, providing critical insights into the barrier properties and the corrosion kinetics.

2.4.5.1. Electrochemical Characterizations

We employed electrochemical measurement to evaluate the corrosion resistance of different coating systems. All tests were conducted using an IVIUnSTAT, a multichannel electrochemical interface, connected to a three-electrode electrochemical cell. This cell configuration included an Ag/AgCl reference electrode (RE), a Ni-Cr wire serving as the counter electrode (CE), and the coated steel sample designated as the working electrode (WE), adhering to standard corrosion assessment protocols, as illustrated in Figure 7.

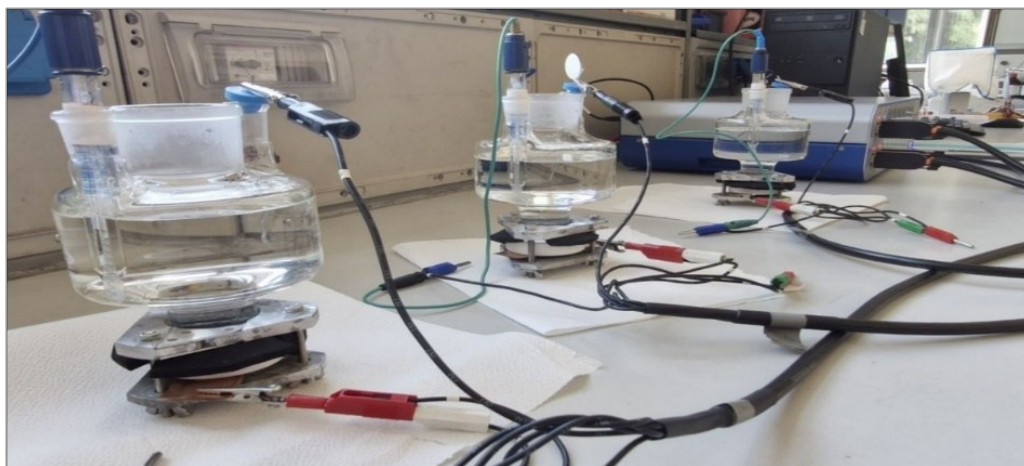


Figure 7 : EIS Setup

To find the optimal film thickness and evaluate the consistency of coating performance, we conducted a series of impedance spectroscopy measurements on samples with varying dry film thicknesses, as indicated in Table 2. In test 4, every coating formulation was subjected to an extra test at near-optimal thickness to guarantee statistical reliability.

Table 2: film thicknesses

| Sample | TEST | Thickness (μm) |
|--------|--------|-----------------------------|
| L0-5 | TEST 1 | 27 |
| | TEST 2 | 54 |
| | TEST 3 | 112 |
| | TEST 4 | 45 |
| L1-5 | TEST 1 | 40 |
| | TEST 2 | 53 |
| | TEST 3 | 179 |
| | TEST 4 | 72 |
| L3-5 | TEST 1 | 41 |
| | TEST 2 | 61 |
| | TEST 3 | 169 |
| | TEST 4 | 57 |

Electrochemical Impedance Spectroscopy (EIS) measurements were conducted over a frequency range from 10^{-2} to 10^4 Hz, employing a sinusoidal signal with an amplitude of 10 mV. To achieve sufficient resolution across the spectrum, 10 data points per frequency decade were recorded. All experiments were carried out in a 3.5 Wt.% NaCl solution at room temperature, chosen to mimic chloride-rich conditions commonly found in marine or coastal environments. The area of the exposed working electrode was 0.785 cm^2 , and all impedance results were normalized to reflect an equivalent area of 1 cm^2 .

Measurements started one hour after immersion in the electrolyte and were conducted every 24 hours for about 14 days to assess the coatings' long-term protective performance and stability.

The impedance spectra obtained were further analyzed using equivalent electrical circuit (EEC) modeling, which helps in characterizing the interfacial behavior between the metal substrate and the coating. This approach allows for interpreting the corrosion mechanism by connecting physical phenomena with electrical circuit elements, thus enabling the observation of changes in system parameters over immersion time.

2.4.5.2. Principle of Equivalent Electrical Circuit Modeling

When an AC voltage is applied to an electrochemical cell, the resulting impedance $Z(\omega)$ is defined as:

$$Z(\omega) = V(\omega) / I(\omega) \quad \text{Equation 1}$$

Where $\omega = 2\pi f$ represents the angular frequency of the applied signal, and $V(\omega)$ and $I(\omega)$ denote the applied voltage and measured current, respectively. These sinusoidal signals can be represented as:

$$V(t) = V_m \sin(\omega t) \quad \text{Equation 2}$$

$$I(t) = I_m \sin(\omega t - \varphi) \quad \text{Equation 3}$$

Here, V_m and I_m are the maximum amplitudes, and φ is the phase shift between voltage and current. Using Euler's relation, sinusoidal functions can be rewritten in exponential form:

$$V(t) = V_m e^{j\omega t} \quad \text{Equation 4}$$

$$I(t) = I_m e^{j(\omega t - \varphi)} \quad \text{Equation 5}$$

Thus, the complex impedance becomes:

$$Z(\omega) = \frac{V_m}{I_m} e^{(j\varphi)} = Z_0 (\cos \varphi + j \sin \varphi) \quad \text{Equation 6}$$

Where $Z_0 = \frac{V_m}{I_m}$ is the magnitude of the impedance, which can also be expressed as:

$$Z(\omega) = Z_0 \cos \varphi + j Z_0 \sin \varphi \quad \text{Equation 7}$$

In this context, the real part corresponds to resistance, while the imaginary part represents reactive components, such as capacitance and inductance. EIS data are visualized using Bode plots (impedance magnitude and phase vs. frequency) and Nyquist plots (real (Z') the opposite of imaginary impedance(Z'')).

The system's electrical behavior is often modeled using equivalent electrical circuits (EEC). A typical model features a series resistance (solution resistance, R_s) in conjunction with a parallel arrangement comprising the coating resistance, R_{coat} , a constant phase element (CPE_{coat}), the charge transfer resistance (R_{CT} , and an additional CPE for the double-layer capacitance (CPE_{dl}). This configuration accurately captures impedance spectra showing two time constants. (Figure 8). The CPE replaces the ideal capacitor in the model to capture non-ideal capacitive behavior due to surface heterogeneity. Its impedance is expressed as:

$$Z_{CPE} = 1/Q(j\omega)^n \quad \text{Equation 8}$$

Where:

- Q is the pseudo-capacitance (units of $\Omega^{-1}s^n$)
- n is a dimensionless exponent ($0 < n \leq 1$); $n=1$ indicates ideal capacitive behavior and $n=0$ acts as a pure resistor.

The coating resistance(R_{coat}) indicates the barrier effectiveness, while the charge transfer resistance (R_{CT}) reflects the corrosion rate at the metal-coating interface. High values of both parameters suggest better corrosion protection.

Electrical circuits are used to model the EIS data

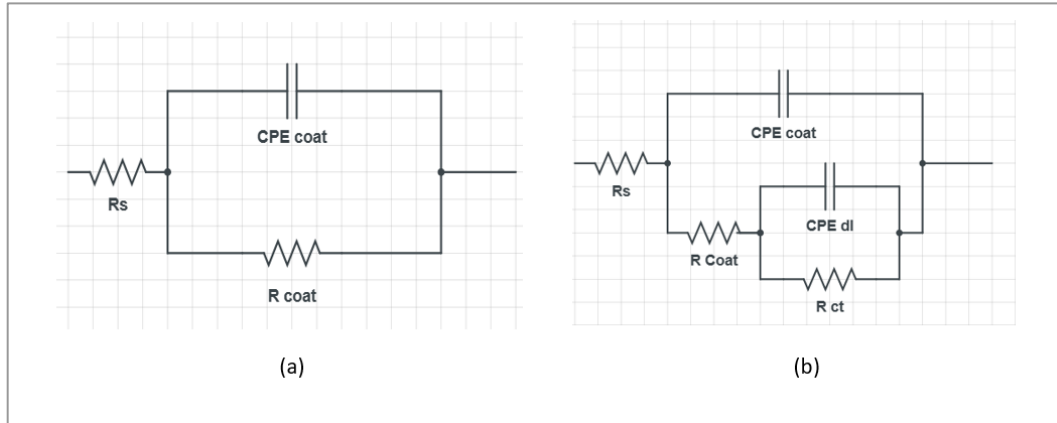


Figure 8 .:

The time constant associated with a particular RC circuit is given by:

$$\tau = R \cdot C \quad \text{Equation 9}$$

And the capacitance of a dielectric layer is calculated as:

$$C = \epsilon_0 \epsilon_r A / d \quad \text{Equation 10}$$

Here, ϵ_0 refers to vacuum permittivity, ϵ_r Indicates relative permittivity, A denotes area, and d represents dielectric thickness.

Electrochemical Impedance Spectroscopy (EIS) permits the observation of degradation phenomena such as water absorption, delamination, and ions diffusion. Monitoring the changes in impedance parameters during immersion gives crucial insights into the durability of coatings. The parameters during immersion provide key data on coating durability.

2.4.6. Field Emission Scanning Electron Microscopy (FE-SEM)

The SEM images served to assess the coating morphology and structural modifications subsequent to immersion in the NaCl electrolyte solution after the corrosion test.

To facilitate high-resolution SEM imaging by reducing surface charging and ensuring uniform secondary electron emission, steel samples were sputter-coated with a thin platinum layer using a Quorum Q150TS Sputter Coater (operated at 30 mA for 20 s, under argon).

Surface morphology of the coated steel samples following corrosion testing was examined using a Zeiss SUPRA 40 Field Emission Scanning Electron Microscope (FE-SEM). Samples were mounted on SEM stubs with carbon tape and imaged under high vacuum conditions at accelerating voltages ranging from 5 to 15 kV.

4. Results and Discussion

This chapter discusses the results of the characterization analyses introduced in Chapter 2, specifically emphasizing the corrosion resistance of lignin-based coatings. Electrochemical measurements were conducted on coatings created with epoxidized soybean oil and various lignin concentrations to evaluate the effect of lignin content and find the optimal level for corrosion protection.

The chapter concludes with an exploration of the characterization of photocurable formulations. Here, ATR-FTIR spectroscopy is employed to verify successful photo-crosslinking, followed by an analysis of the thermomechanical properties of the different resin formulations.

4.1. UV-Curing Process

The photocuring process was followed by measuring the conversion of epoxy groups. Upon UV exposure, ring-opening of epoxy groups is initiated. FTIR was performed to observe the chemical changes during this curing process.

As shown in Figure 9, adding lignin to epoxidized soybean oil did not cause a significant shift in the peak positions of the FTIR spectra, indicating no significant alteration in the chemical structure of the ESO matrix. However, the absorption peak intensities related to C=C stretching vibrations in aromatic rings are notably near 1600 cm^{-1} became more prominent with increasing lignin content, especially in the 3 wt.% lignin formulation. This enhanced intensity reflects the higher aromatic ring introduced by lignin. The FTIR spectra displayed several significant vibrational bands linked to the functional groups in the ESO-based resin. In particular, absorption peaks at 2926 cm^{-1} and 2854 cm^{-1} corresponded to the asymmetrical and symmetrical stretching vibrations of methylene ($-\text{CH}_2-$) groups. A prominent band at 1745 cm^{-1} is linked to the stretching vibration of ester carbonyl ($\text{C}=\text{O}$) groups, which play a vital role in the ESO structure. Additional peaks at 1465 cm^{-1} and 1387 cm^{-1} were detected, representing the scissoring and rocking modes of C-H bonds in CH_2 and CH_3 groups. The range between 1162 cm^{-1} and 1116 cm^{-1} is attributed to C-O bending and stretching vibrations, respectively. A particularly notable signal at 840 cm^{-1} signifies epoxy ring, an essential marker for tracking the epoxy conversion process.

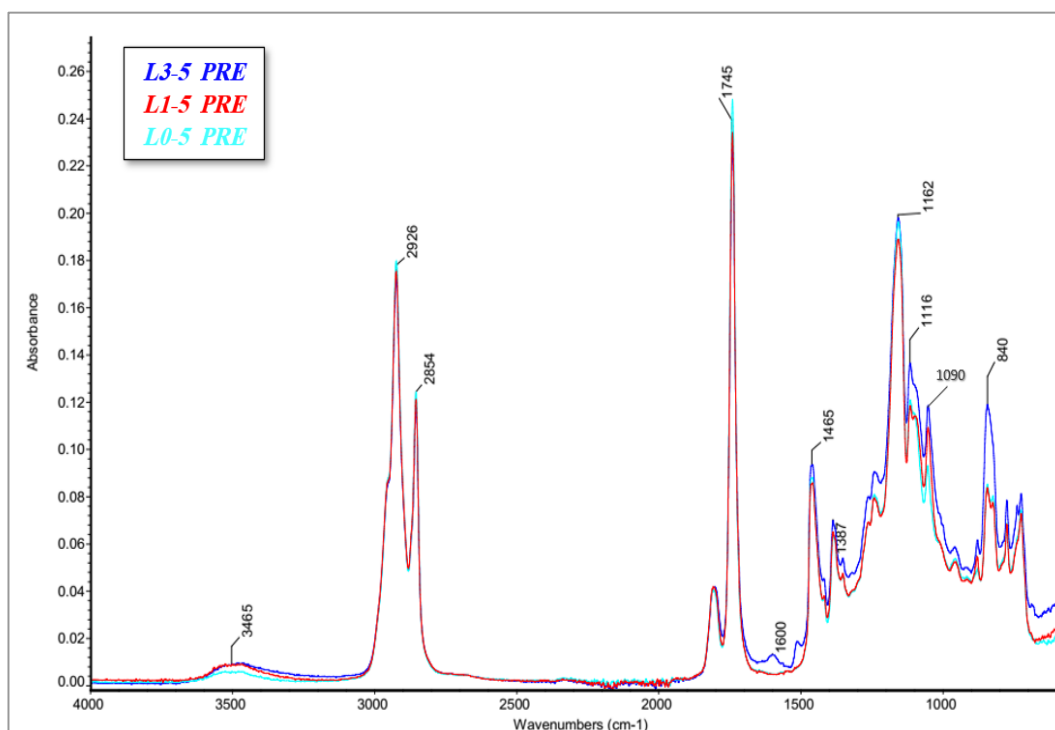


Figure 9: FTIR spectra of uncured ESO-based formulation containing 0%, 1%, and 3% wt. lignin.

After UV curing, as shown in Figure 10, a notable reduction in the 840 cm^{-1} peak was observed, confirming the effective opening of the epoxy ring. Concurrently, two new absorption peaks appeared: one at 1090 cm^{-1} associated with ether linkages, and another broad band near 3465 cm^{-1} , corresponding to O–H stretching vibrations, which indicates the formation of hydroxyl groups as a consequence of the ring-opening process. The results for the 11 wt.% Ph. I formulation is shown in Figure 11 as a representative example to evaluate how lignin content affects the conversion of epoxy groups. Among the samples tested, the formulation with 1% lignin exhibited the highest crosslinking efficiency, suggesting that lignin enhances the cationic curing reaction. This improvement is likely due to lignin's phenolic and hydroxyl functional groups, which can engage in polymerization reactions, enhancing lignin's reactivity within polymer matrices, promoting crosslinking, and enhancing the cured materials' structural integrity or stabilizing the reactive cationic intermediates formed during photoinitiation. In contrast, the formulation containing 3 wt.% lignin (L3-11) showed lower conversion at both early and final irradiation times than L1-11. This reduced reactivity is attributed to lignin's UV shielding effect. Lignin can absorb or scatter incoming light, limiting photo-initiator activation and reducing polymerization efficiency.

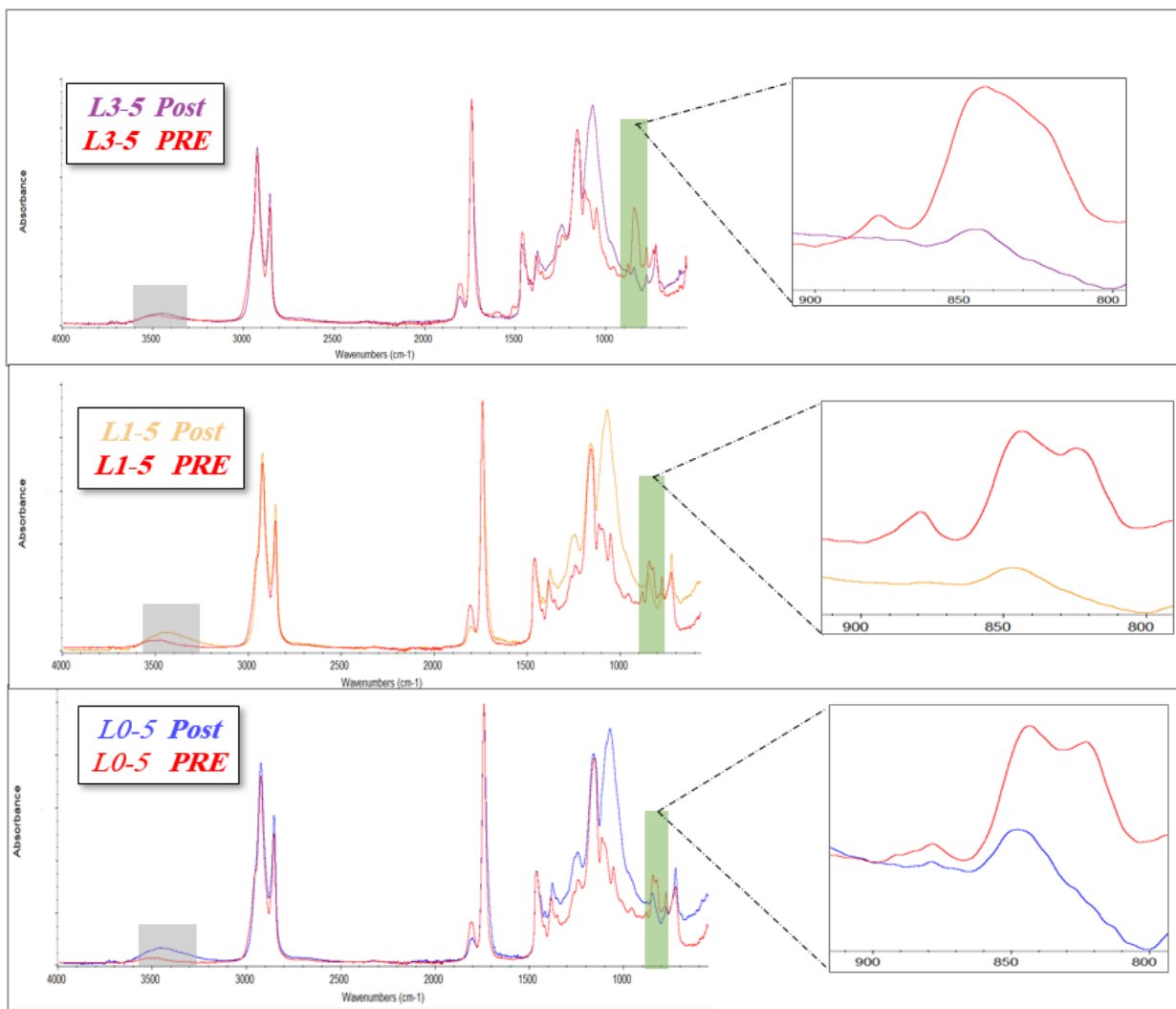


Figure 10 : FTIR-T spectra before and after UV curing of ESO and ESO composites.

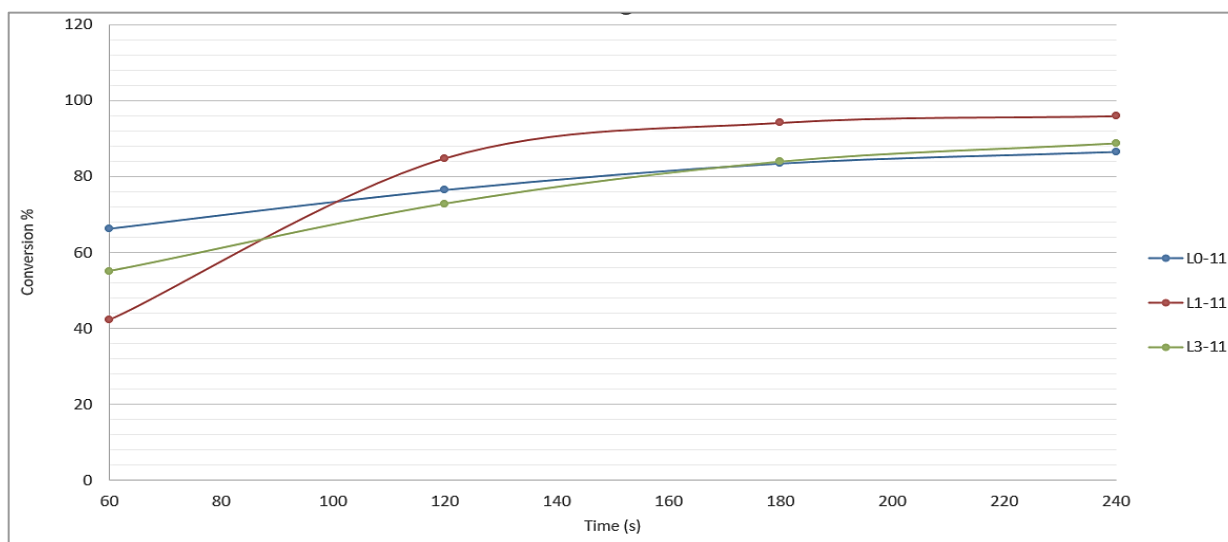


Figure 11 : FTIR-T Epoxy conversion (%) over UV exposure time of formulations with varying lignin content.

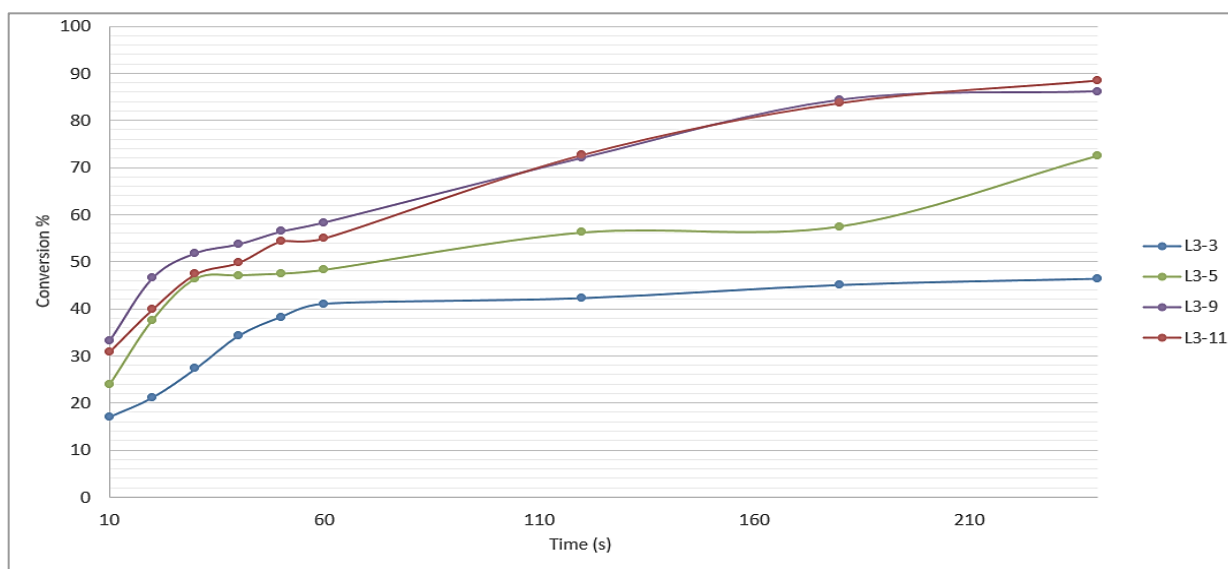


Figure 12: FTIR-T Epoxy conversion (%) of formulations with varying photo initiator content at different irradiation times.

Findings from the investigation of the 3 wt% lignin formulation at different PhI concentrations are illustrated in Figure 12. The results indicate that the formulations with 9 wt% and 11 wt% PhI achieve the highest levels of epoxy conversion, reflecting effective photoinitiation and propagation of the cationic curing reaction at these concentrations. However, elevated levels of ionic photo-initiators can increase the ionic content of the cured film, which is known to promote water uptake and accelerate corrosion in coating systems, despite the higher curing efficiency obtained with 9%

and 11% PhI, the 5% PhI formulation was chosen as the optimal balance, offering sufficient photocuring efficiency while minimizing the corrosion promotion associated with higher photoinitiator loadings. Epoxy conversion of L0-5, L1-5, and L3-5 after coating is reported below in Table 3.

Table 3: FTIR-ATR Epoxy conversion (%) with 5% PhI of coated films after UV curing.

| Sample | conversion % |
|--------|--------------|
| L0-5 | 64.20 |
| L1-5 | 85.39 |
| L3-5 | 78.68 |

4.2. Viscosity Evaluation

The viscosity of photocurable resin plays a vital role in determining its appropriateness for coating applications, as rheological properties greatly influence both processability and overall performance. Figure 13 demonstrates that formulation L3-5 exhibited Newtonian behavior throughout the tested shear rate range, maintaining a nearly constant viscosity. In contrast, L0-5 and L1-5 displayed typical shear-thinning behavior, where viscosity decreased progressively as the shear rate increased, ultimately stabilizing at a consistent value in the high-shear region, known as the second Newtonian plateau.

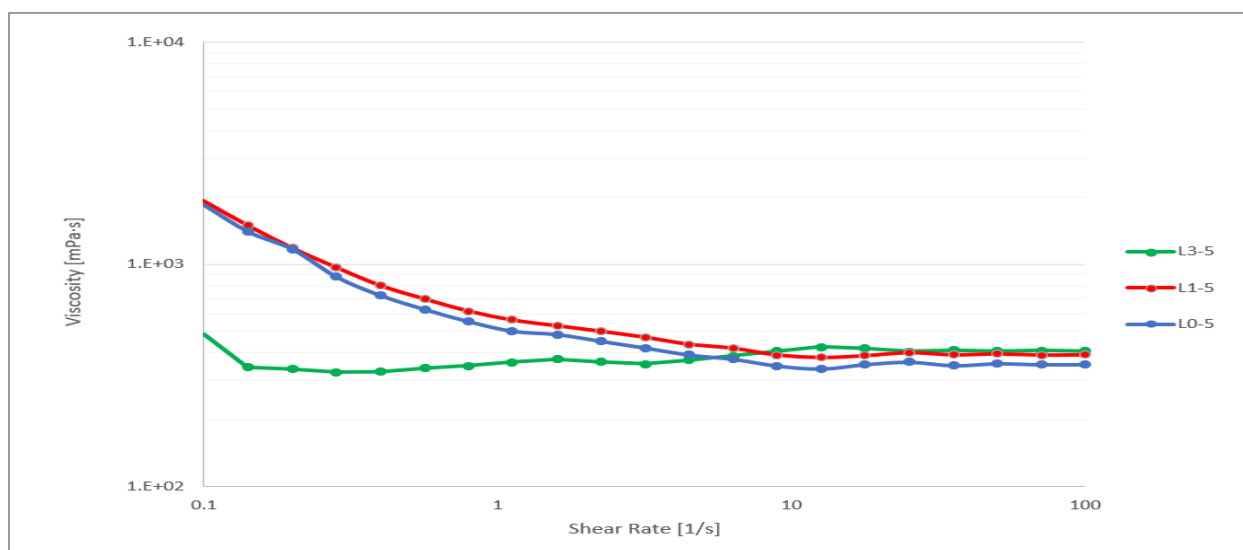


Figure 13 Viscosity curve

The rheological behaviors of samples L0-5 and L1-5 were well-represented by the Sisko model (Equation 2), whereas the L3-5 sample was more suitably described by the Power Law model (Equation 1). Detailed viscosity model parameters for each sample can be found in Table 4. L0-5 and L1-5 showed low flow behavior index values, with $n = 0.04$ and 0.08 , respectively. In contrast, L3-5 exhibited a flow index near 1.0 , indicating its Newtonian behavior, with an average viscosity of $411 \text{ mPa}\cdot\text{s}$. In summary, the flow behavior index n increases with lignin loading, suggesting that lignin enhances chain flexibility and contributes to the rise in n .

Table 4: Viscosity model parameters.

| | Fitting Model | K | n | $\eta^\infty [\text{mPa}\cdot\text{s}]$ | $\eta [\text{mPa}\cdot\text{s}]$ |
|------|---------------|------|------|---|----------------------------------|
| L0-5 | Sisko | 0.17 | 0.04 | 349.7 | 353 |
| L1-5 | Sisko | 0.18 | 0.08 | 387.6 | 390 |
| L3-5 | Power law | 0.37 | 1 | - | 411 |

4.3. Photo-rheology

The changes in storage and loss moduli due to UV irradiation were monitored using photo-rheology, which provided insights into curing behavior and kinetics after light activation, as shown in Figure 14.

As demonstrated in Table 5, the onset time of G' was observed to extend with higher lignin content. L1-5 showed a minor delay relative to the pristine formulation, increasing from 40 to 50 seconds, whereas L3-5 took 75 seconds to initiate network formation, almost doubling the time required by the lignin-free system. This trend indicates that lignin might hinder light transmission by absorbing or scattering UV light, thus reducing photo-initiators' activation and postponing the onset of polymerization. A similar observation was made regarding gelation time, where the L3-5 took 177 seconds to reach the gel point, which is more than twice the time needed by the pristine sample, which gelled in 78 seconds. Moreover, the kinetics of photopolymerization, indicated by the slope of the G' curve, decreased with the addition of lignin. L1-5 showed a moderate reduction,

while L3-5 's rate fell to about one-third of the initial rate. These results demonstrate that while small amounts of lignin can be compatible with UV-curable ESO systems, excessive amounts slow the curing kinetics and delay network formation by limiting light exposure and decreasing the overall reactivity of the formulation.

Table 5: Parameters of the photo-polymerization of ESO formulations.

| | Onset Time (s) | Gelation Time (s) | $\Delta G'/\Delta t$ (Pa/s) |
|------|----------------|-------------------|-----------------------------|
| L0-5 | 40 | 78 | 597 |
| L1-5 | 50 | 109 | 560 |
| L3-5 | 75 | 177 | 184 |

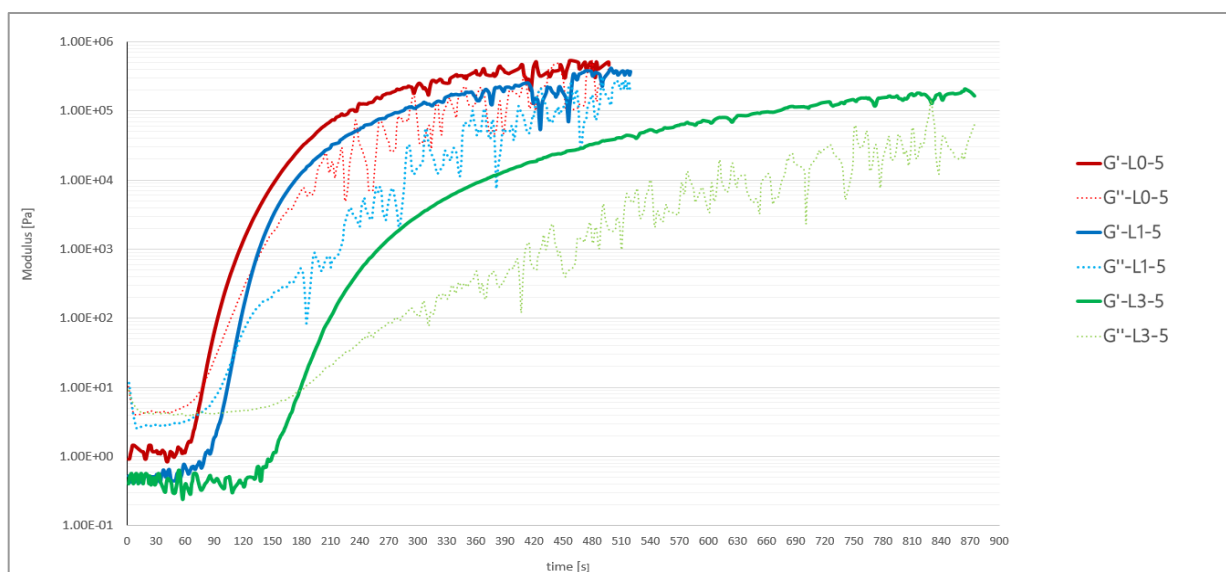


Figure 14: Photo-rheology Curves.

4.4. Curing Behavior

Differential Scanning Calorimetry (DSC) assessed the formulations' thermal properties. As shown in Figure 15, the DSC thermograms showed a minor exothermic peak in both L0-5 and L3-5 samples during the initial heating cycle, suggesting residual curing. A higher lignin content is

linked to a higher glass transition temperature (Table 6), indicating enhanced thermal stability and a more rigid polymer network.

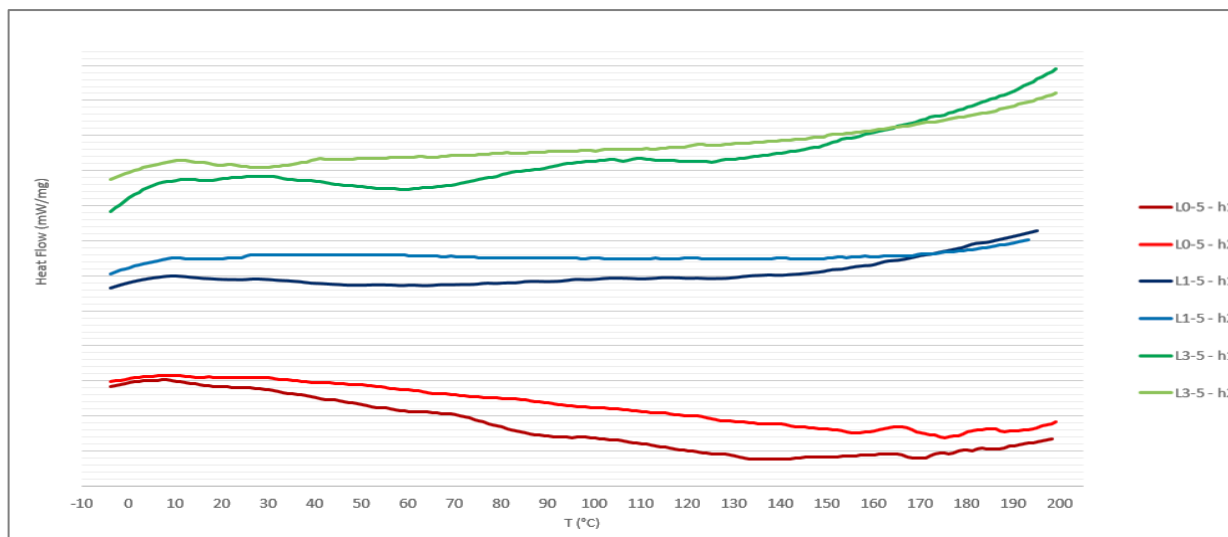


Figure 15 : DSC thermograms of formulations.

The L0-5 sample had the lowest Tg, while L3-5, with 3% lignin, exhibited the highest Tg and a noticeable increase between the first and second heating cycles. This Tg change indicates that L3-5 experienced post-curing during thermal treatment due to unreacted epoxy groups in photopolymerization and hydroxyl groups from lignin, which enhance crosslinking.¹⁷ In contrast, the L1-5 sample showed no significant Tg change during the heating cycles, indicating thorough epoxy conversion during initial UV curing and minimal remaining reactivity. These findings suggest that thermal curing significantly impacts systems with lower initial epoxy conversion.

Table 6 : Glass transition temperatures of formulations in the first and second heating cycles.

| Sample | Tg-h1 (°C) | Tg-h2 (°C) |
|--------|------------|------------|
| L0-5 | 11.28 | 13.28 |
| L1-5 | 12.28 | 12.28 |
| L3-5 | 14.28 | 18.28 |

4.5. TGA

Thermal degradation characteristics of the formulations were analyzed using thermogravimetric analysis. As illustrated in Figure 16 and summarized in Table 7, the L0-5 epoxidized soybean oil sample showed a $T_{5\%}$ around 282.9 °C and a T_{peak} near 387.28 °C, with a char residue of 0.08%. The L1-5 sample, containing 1% lignin, had slightly lower $T_{5\%}$ and T_{peak} values, indicating an earlier degradation onset. Conversely, the L3-5 sample with 3% lignin displayed higher $T_{5\%}$ (277.08 °C) and T_{peak} (383.75 °C), along with the greatest char residue of 0.22%. This enhancement is due to lignin's aromatic structure promoting char formation during decomposition. These findings suggest a nonlinear, yet stabilizing, effect of lignin: lower concentrations may speed up degradation, while higher content (3%) helps restore or enhance thermal stability, highlighting lignin's protective role at high temperatures.

Table 7: TGA parameters

| | $T_{5\%}$ (°C) | T_{Peak} (°C) | Char Residue (%) |
|------|----------------|-----------------|------------------|
| L0-5 | 282.9 | 387.28 | 0.08 |
| L1-5 | 273.43 | 375.37 | 0.15 |
| L3-5 | 277.08 | 383.75 | 0.22 |

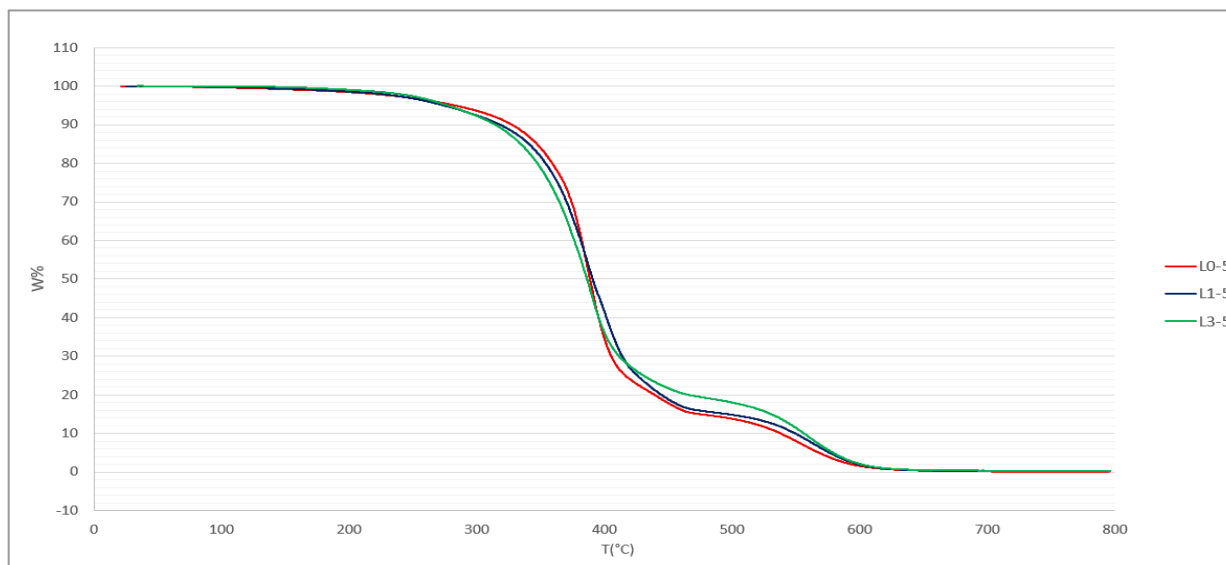


Figure 16: TGA curves of ESO and ESO composite.

4.6. Coating Hardness

The pencil hardness test was conducted to examine the coatings' surface characteristics. Sample L0-5 displayed the lowest hardness, rated as B, which indicates a softer surface. In Sample L1-5, the hardness improved to H and increased to 2H in Sample L3-5, demonstrating enhanced surface rigidity attributed to the incorporation of lignin.

4.7. Contact Angle Measurement

The results of the dynamic wettability tests in Table 8, show that adding lignin to ESO-based coatings changes surface characteristics based on the concentration and the type of test liquid used. The L0-5 sample displayed moderate hydrophobicity, as shown by water contact angle measurements. Adding 1% lignin (L1-5) resulted in a slight decrease in the contact angle, indicating better wettability. However, increasing the lignin concentration to 3% (L3-5) caused the contact angle to rise, exceeding the value recorded for the neat ESO sample, which indicates a rise in hydrophobicity. This suggests that lower lignin concentrations promote hydrophilicity, while higher levels enhance hydrophobicity, depending on how they interact with the contacting fluid. This observation aligns with previous research showing that lignin is naturally hydrophilic due to its many polar structures. Typical water contact angles (WCAs) for coatings containing lignin average around 80°, but with proper adjustments in surface morphology and composition, WCAs can surpass 90°, indicating a transition towards hydrophobicity behavior.³⁹

For glycerol, a more polar liquid, the opposite trend was noted. L0-5 demonstrated the highest contact angles, whereas L1-5 and L3-5 indicated better spreading and lower contact angles. This implies that the polar functional groups of lignin improve surface compatibility with polar solvents, highlighting lignin's amphiphilic nature. These results further confirm lignin's dual function in modifying surface energy based on its concentration and the polarity of the interacting liquid.⁴⁰

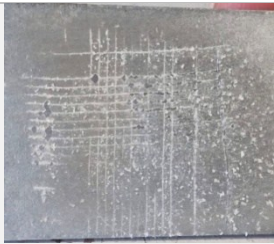


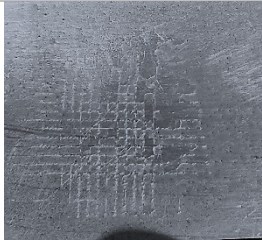
Table 8 : Measurements of contact angles of coatings using water and glycerol.

| | water | Glycerol |
|-----------|---------------|---------------|
| Sample No | Contact Angel | Contact Angel |
| L0-5 | 78.19 | 86.57 |
| L1-5 | 75.43 | 79.02 |
| L3-5 | 84.61 | 78.8 |

4.8. Coating Adhesion

The adhesion performance of the three coatings was assessed using the cross-cut tape test, with results reported in a table based on ASTM D3359-B standard, as detailed in Table 9. Sample L0-5 showed significant coating loss, with large sections of the lattice detached, leading to a 1B rating and indicating poor adhesion. L1-5 showed moderate coating retention with partial flaking along the cut edges, matching a 3B rating that suggests fair adhesion. Conversely, L3-5 demonstrated superb adhesion, with no visible detachment or edge lifting, earning a 5B rating.

Table 9: Results of the adhesion test for coating samples.

| Samples | Before | After Tape Removal | ASTM Class |
|---------|---|--|------------|
| L0-5 |  |  | 1B |
| L1-5 |  |  | 3B |



4.9. Solvent Resistance

The solvent rub test using toluene revealed that the L0-5 sample, which contains the ESO coating, withstood 11 double rubs before visible degradation occurred. In comparison, the L1-5 sample endured 25 double rubs, while the L3-5 sample resisted up to 23 double rubs. These results suggest that both L1-5 and L3-5 exhibited greater solvent resistance than L0-5 under the same test conditions.

4.10. Electrochemical Impedance Spectroscopy Measurements

The corrosion behavior of coatings has been investigated using Electrochemical Impedance Spectroscopy (EIS). The results indicate that thinner coatings do not exhibit sufficient anti-corrosive properties in electrolytes containing chlorides. Figures 17 present the outcomes of test 2, featuring samples with an average thickness of 55 μm , illustrated as Bode diagrams. Initially, after one hour of immersion in the solution, the coatings containing 3% lignin exhibited good protective behavior. A capacitive response is observed at high frequencies, as indicated by phase angle values approaching 90° . This behavior transitions to a resistive response at low frequencies, where the impedance modulus ($|Z|$) attains a plateau.

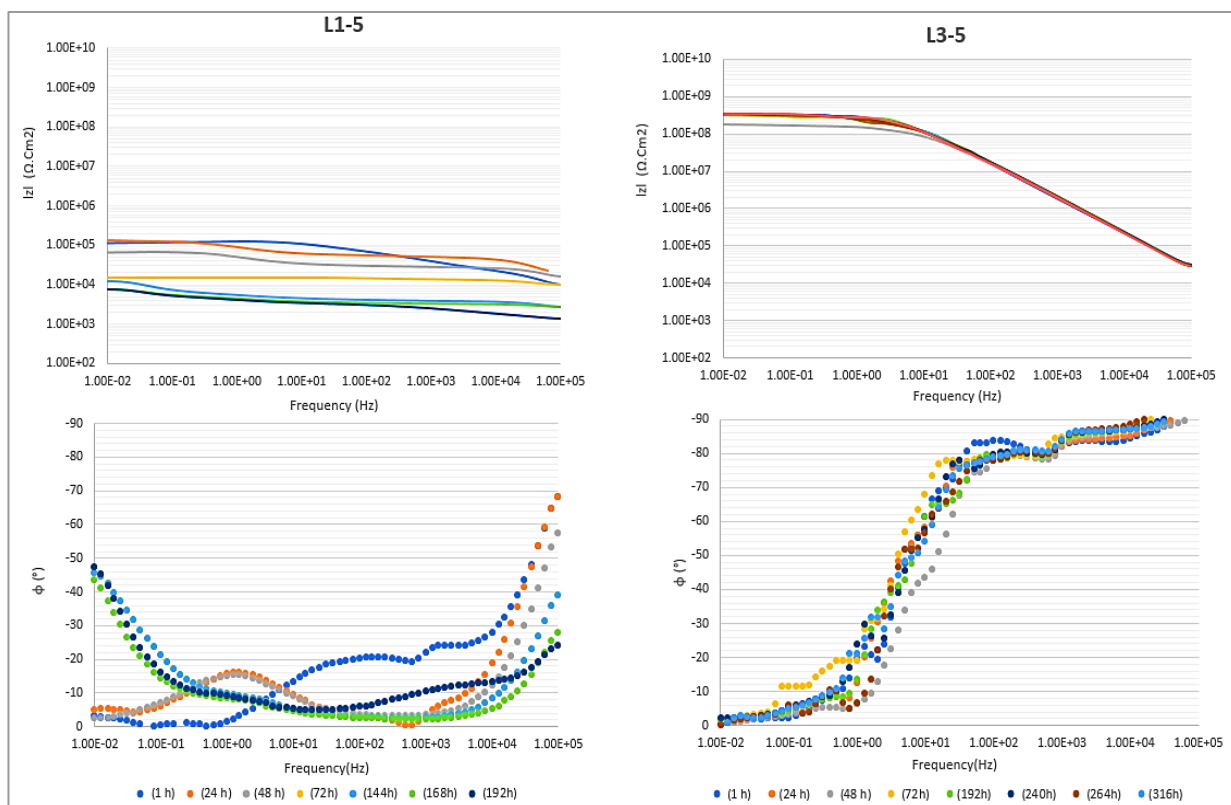


Figure 17: Impedance spectra of test 2, presented as Bode diagrams, were acquired for the coatings as a function of the immersion time in the 3.5 % NaCl solution.

The L3-5 samples exhibit the highest impedance modulus values, indicating strong protective properties, peaking at $3.17 \times 10^8 \Omega \cdot \text{cm}^2$. In contrast, the L1-5 samples demonstrate intermediate protective capacity, with impedance values around $4.74 \times 10^5 \Omega \cdot \text{cm}^2$. As indicated in Figure 18, the L0-5 samples show the lowest impedance values, remaining below $1 \times 10^4 \Omega \cdot \text{cm}^2$ throughout the test. An organic coating is considered non-protective if the impedance modulus falls below $1 \times 10^4 \Omega \cdot \text{cm}^2$ at low frequencies in saline environments.⁴¹

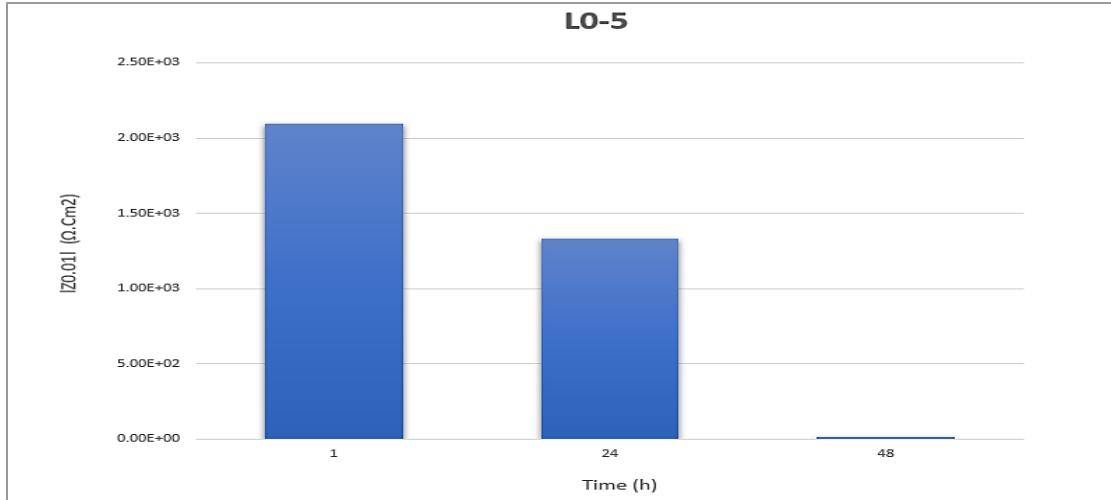


Figure 18 : the impedance modulus ($|Z|$) of L0-5-test2 at a frequency of 0.01 Hz

As immersion time increases, distinct degradation behaviors emerge. Samples L3-5 show a gradual reduction in low-frequency impedance modulus over time but later demonstrate recovery and stabilization near their initial values, indicating improved long-term stability. Samples L1-5 display a notable decrease in impedance modulus within just 24 hours, with an ongoing decline noted until the end of the test, ultimately reaching $7.70 \times 10^3 \Omega \cdot \text{cm}^2$, which indicates no protective effectiveness. This degradation is further evidenced by the phase angle dropping below 50° throughout the frequency spectrum. The reproducibility test 4 on samples of similar thickness confirmed consistent results and trends across all three formulations.

Since the unmodified ESO coating alone does not exhibit sufficient protective properties, thicker coatings were assessed to improve their anticorrosion efficacy. All samples tested with increased thickness underwent electrochemical impedance spectroscopy in test 3. The experimental results, as anticipated, confirmed that the performance of corrosion protection was significantly affected by the thickness of the coating. As thickness increased, the effect of lignin content diminished, leading all coatings to exhibit excellent barrier properties. In Figure 19, this is evident from the impedance modulus at 0.01 Hz, which remained consistently around $10^9 \Omega \cdot \text{cm}^2$ throughout the 9 days of immersion. However, when considering economics, enhancing the coating thickness for protection may not be the most cost-effective strategy; thinner alternatives could be improved through formulation adjustments.

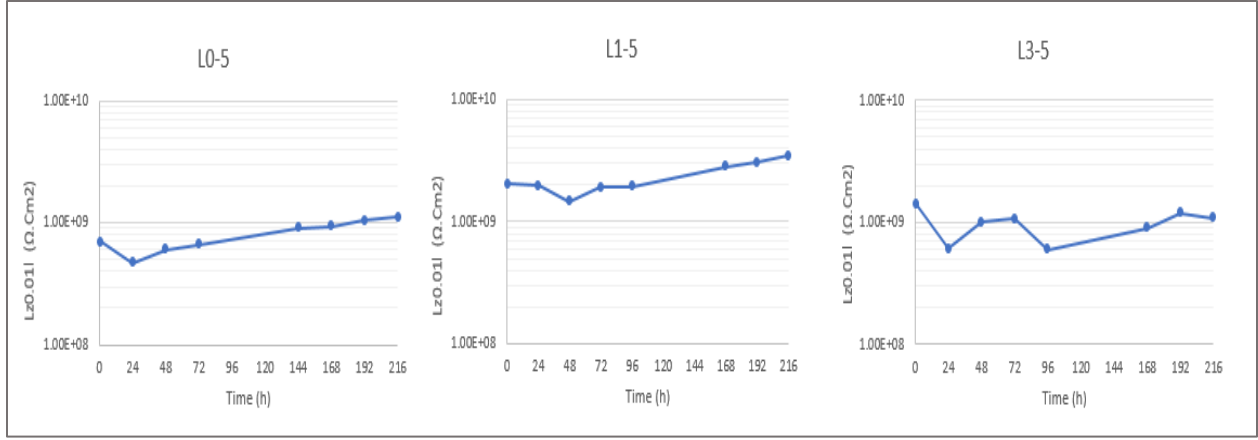


Figure 19 : The impedance modulus for three coatings of test 3 at a frequency of 0.01 Hz.

4.10.1. Modeling of Electrochemical Impedance Spectroscopy Spectra

Equivalent electrical circuit modeling was utilized to better understand the impedance spectroscopy results and develop a quantitative model that illustrates the coating and transport phenomena occurring during the test. The impedance data were analyzed using a simplified circuit in Figure 7(a). Nevertheless, to accurately represent the two-time constants evident in specific spectra, a more complex circuit, as shown in Figure 7(b), was utilized for fitting. Table 10 presents the complete set of parameters obtained from the EEC.

Electrical circuit modeling was performed across the three coatings to evaluate how lignin content affects coating performance. Figures 20,21, and 22 illustrate the results of test 2, indicating that assessments were made after 24 and 316 hours of immersion. The dots indicate the experimental data points, while the lines represent the experimental points from the EEC. For the L0-5 coating, barrier performance was observed to be limited. After 24 hours, its R_{Coat} measured at a relatively low value of $4.01 \times 10^3 \Omega \cdot \text{cm}^2$, while CPE_{Coat} was recorded at $7.07 \times 10^{-9} \text{ s}^n / \Omega \cdot \text{cm}^2$ is indicative of higher dielectric permeability. Additionally, R_{ct} of $1.38 \times 10^4 \Omega \cdot \text{cm}^2$ and CPE_{dl} of $4.17 \times 10^{-4} \text{ s}^n / \Omega \cdot \text{cm}^2$ were noted, accompanied by a n_{dl} of 0.77, suggesting an early onset of interfacial electrochemical activity. However, by 316 hours, the L0-5 coating had failed, confirming degradation and the consequent loss of corrosion protection. In contrast, L1-5 demonstrated significant performance improvements. After 24 hours, R_{Coat} rose to $7.16 \times 10^4 \Omega \cdot \text{cm}^2$, while CPE_{Coat} decreased to $4.7 \times 10^{-10} \text{ s}^n / \Omega \cdot \text{cm}^2$, indicating a denser and more

insulating coating. R_{ct} increased to $7.34 \times 10^4 \Omega \cdot \text{cm}^2$, with CPE_{dl} measured at $2.35 \times 10^{-6} \text{ s}^n/\Omega \cdot \text{cm}^2$ and n_{dl} at 0.92, reflecting a robust resistance to interfacial corrosion compared to the ESO coating. After 316 hours, the coating R_{coat} decreases values below $10^4 \Omega \cdot \text{cm}^2$, although some electrochemical activity at the interface had begun, R_{ct} remained significant at $2.50 \times 10^4 \Omega \cdot \text{cm}^2$, confirming its effective corrosion resistance.

L3-5, containing the highest lignin content, demonstrated the most effective barrier performance. After 24 hours, R_{coat} is significantly higher at 3.19×10^8 and the CPE_{coat} was markedly lower than in other samples, indicating excellent coating integrity that prevented electrolyte penetration and suppressed electrochemical activity at the metal interface. Even after 316 hours, L3-5 maintained this superior performance.

The advantages of higher lignin content become clear when comparing L1-5 and L3-5, as illustrated in the Bode diagram. L1-5 exhibited moderate barrier efficacy after 24 hours, showing some interfacial activity by the end of the assessment, which suggests partial electrolyte access. Conversely, L3-5 consistently displayed denser and more protective coating structures. These findings confirm that incorporating 3% lignin significantly enhances both short- and long-term corrosion resistance compared to formulations with lower lignin concentrations.

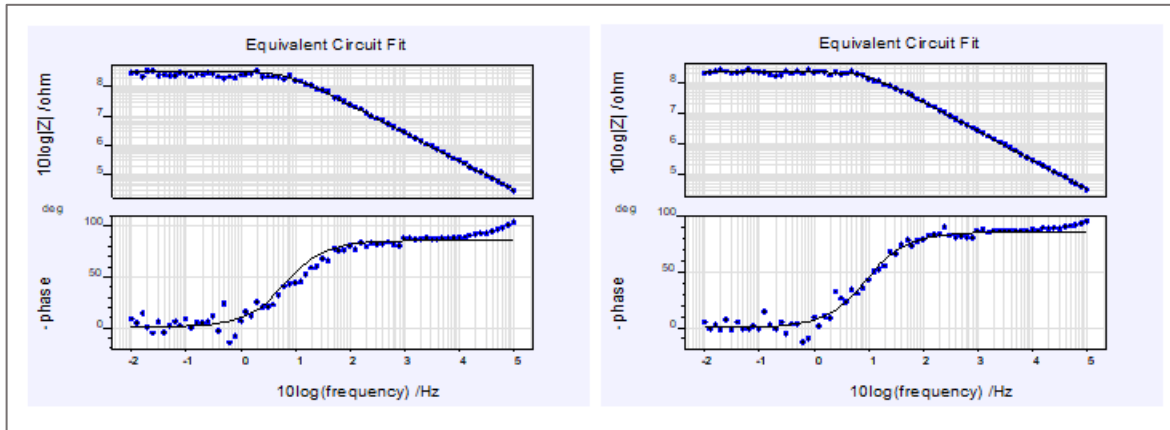


Figure 20: L3-5 24h and 316 h, fitted using equivalent circuit modeling

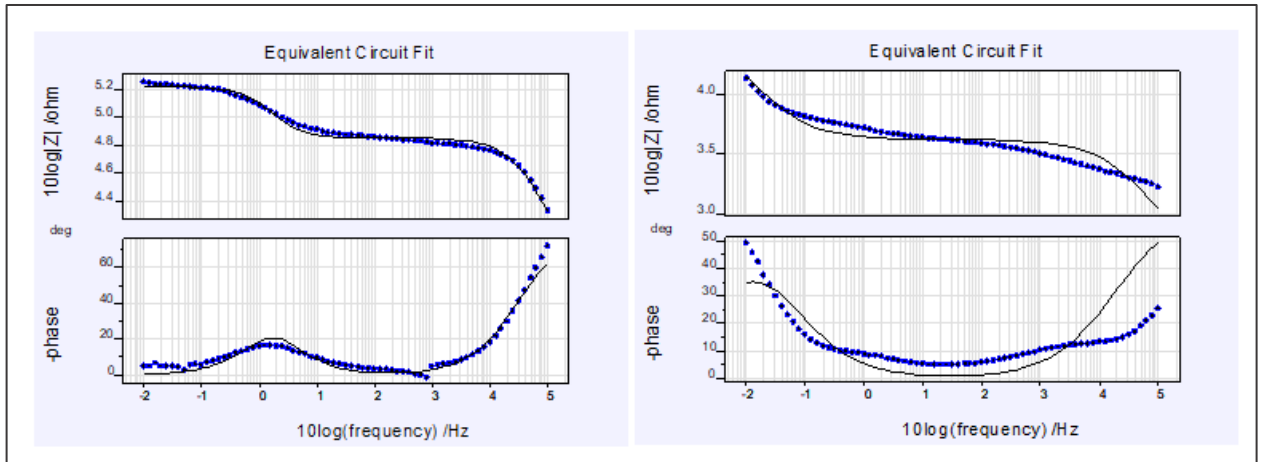


Figure 21: L1-5- 24 h and 316h, fitted using equivalent circuit modeling.

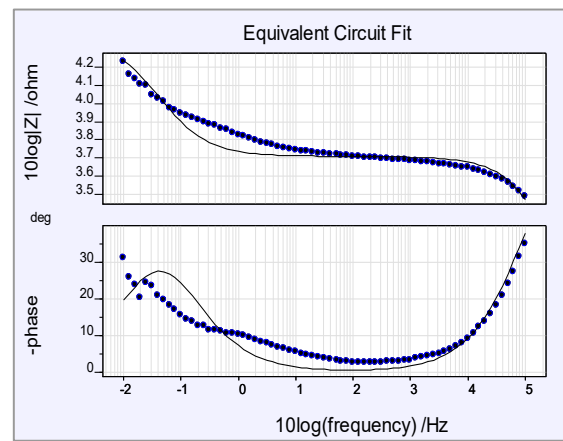


Figure 22: L0-5- 24 h, fitted using equivalent circuit modeling.

| sample | TEST | Thickness | Rs [$\Omega \cdot \text{cm}^2$] | 24 h | | | | | | 336 h | | | | | |
|--------|--------|-----------|--------------------------------------|---|---|----------|---------------------------------------|---|----------|---|---|----------|---------------------------------------|---|----------|
| | | | | Rcoat [$\Omega \cdot \text{cm}^2$] | CPEcoat [$\text{S}^2 \Omega^{-1} \cdot \text{cm}^2$] | n coat | Rct [$\Omega \cdot \text{cm}^2$] | CPEdl [$\text{S}^2 \Omega^{-1} \cdot \text{cm}^2$] | n dl | Rcoat [$\Omega \cdot \text{cm}^2$] | CPEcoat [$\text{S}^2 \Omega^{-1} \cdot \text{cm}^2$] | n coat | Rct [$\Omega \cdot \text{cm}^2$] | CPEdl [$\text{S}^2 \Omega^{-1} \cdot \text{cm}^2$] | n dl |
| L0-5 | TEST 1 | 27 | 10 | Failed | | | | | | | | | | | |
| | TEST 2 | 54 | 10 | 4.01E+03 | 7.07E-09 | 7.93E-01 | 1.38E+04 | 4.17E-04 | 7.65E-01 | Failed | | | | | |
| | TEST 3 | 112 | 10 | 4.64E+08 | 1.02E-10 | 9.62E-01 | -- | -- | -- | 8.78E+08 | 1.48E-10 | 9.25E-01 | -- | -- | -- |
| | TEST 4 | 45 | 10 | Failed | | | | | | | | | | | |
| L1-5 | TEST 1 | 40 | 10 | 1.64E+04 | 2.86E-10 | 9.76E-01 | 7.93E+03 | 1.64E-04 | 9.07E-01 | 1.12E+03 | 2.11E-07 | 7.00E-01 | 2.18E+04 | 5.86E-04 | 7.67E-01 |
| | TEST 2 | 53 | 10 | 7.16E+04 | 4.70E-10 | 8.73E-01 | 7.34E+04 | 2.35E-06 | 9.24E-01 | 3.31E+03 | 8.01E-08 | 7.06E-01 | 2.50E+04 | 7.12E-04 | 7.29E-01 |
| | TEST 3 | 179 | 10 | 1.67E+09 | 4.15E-11 | 9.57E-01 | -- | -- | -- | 3.34E+09 | 6.07E-11 | 9.45E-01 | -- | -- | -- |
| | TEST 4 | 72 | 10 | 1.96E+04 | 1.44E-09 | 8.46E-01 | 1.77E+04 | 1.73E-06 | 8.66E-01 | 1.61E+03 | 2.83E-09 | 9.05E-01 | 2.18E+04 | 5.70E-04 | 7.96E-01 |
| L3-5 | TEST 1 | 41 | 10 | Failed | | | | | | | | | | | |
| | TEST 2 | 61 | 10 | 3.19E+08 | 1.90E-10 | 9.22E-01 | -- | -- | -- | 3.45E+08 | 1.85E-10 | 9.24E-01 | -- | -- | -- |
| | TEST 3 | 169 | 10 | 7.85E+08 | 2.19E-10 | 8.76E-01 | -- | -- | -- | 5.27E+08 | 2.27E-10 | 8.96E-01 | -- | -- | -- |
| | TEST 4 | 57 | 10 | 2.59E+08 | 1.12E-10 | 9.57E-01 | -- | -- | -- | 1.89E+08 | 1.13E-10 | 9.55E-01 | -- | -- | -- |

Table 10 : EEC parameters computed from the EIS spectra acquired on the three coatings.

4.11. FE-SEM Imaging

Figure 23 shows FE-SEM images of the surface morphology for coatings L0-5, L1-5, and L3-5 after Electrochemical Impedance Spectroscopy measurements. The L0-5 sample has extensive surface degradation, with the left image showing severe coating failure in the corrosion area and the right image revealing dense iron oxide clusters, indicating substrate corrosion and poor barrier protection. In contrast, the L1-5 coating shows moderate improvement, with both images displaying surface degradation and visible degraded areas with embedded corrosion products. The microstructure appears to be a degraded polymer matrix mixed with iron oxide, suggesting partial protection but ongoing corrosion. The L3-5 sample, however, remains mostly intact, with only water absorption effects and salt crystals observed on the surface, indicating excellent barrier performance and corrosion resistance.

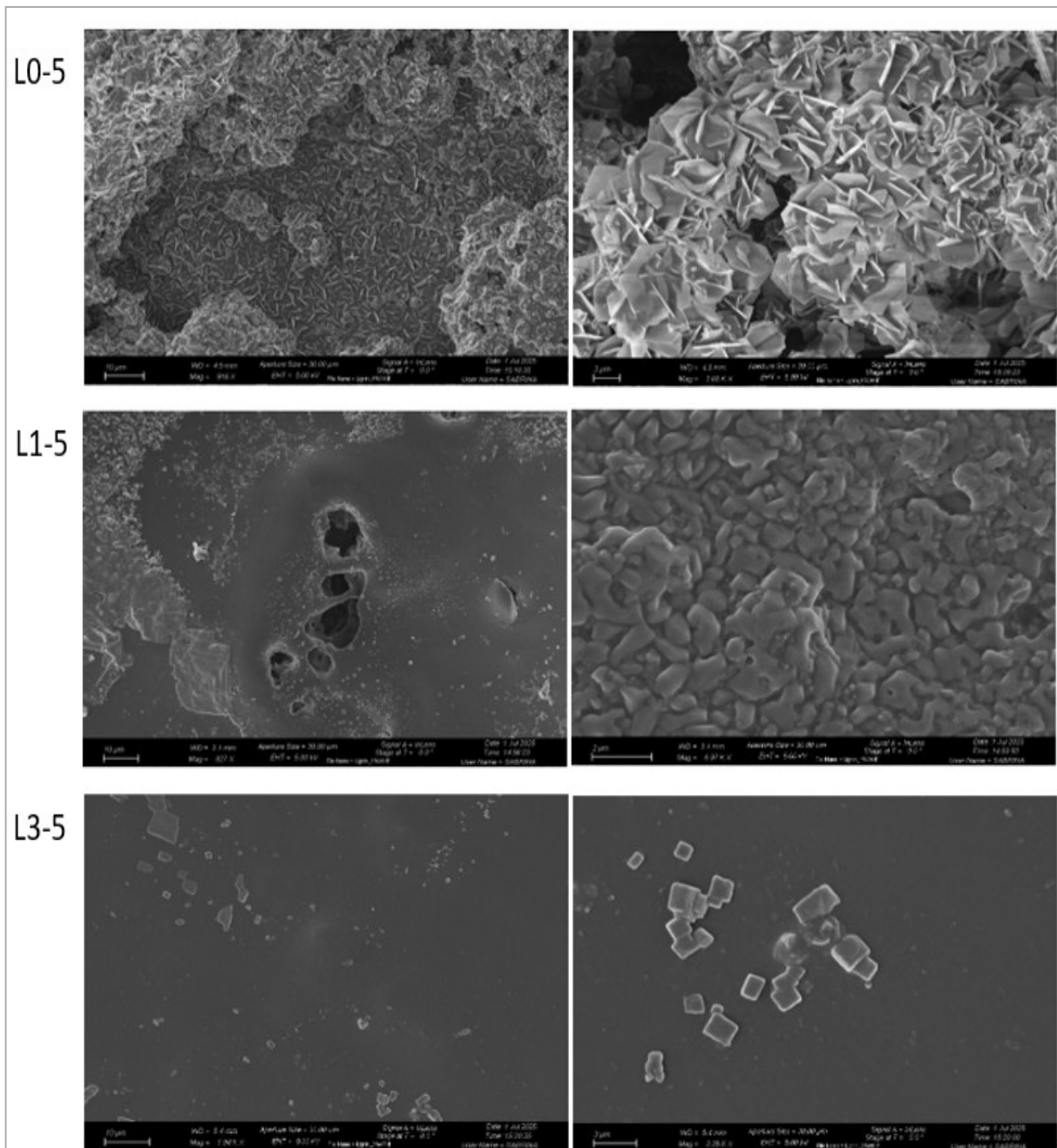


Figure 23: FE-SEM images of L0-5, L1-5, and L3-5 coatings after immersion in 3.5% NaCl solution, shown at low (10 μm) and high magnifications (2–3 μm)

5. Conclusion

This thesis investigated the development of UV-curable coatings based on epoxidized soybean oil (ESO) and lignin for enhanced corrosion protection. The coatings were cured using a cationic photo-initiator to enable solvent-free and energy-efficient crosslinking. The coating properties, including hardness, adhesion, and solvent resistance as well as corrosion properties, based on the research objectives outlined in Section 1.4, are measured, and the results obtained, the following conclusions can be drawn:

- FTIR confirmed high epoxy conversion, while Photo-rheology was employed to evaluate curing kinetics, revealing that higher lignin content led to delayed gelation times and lower kinetics, due to the UV absorption properties of lignin. The cationic photoinitiator optimization was crucial for achieving high conversion rates with well-crosslinked structures, especially in formulations containing lignin.
- Thermal properties were assessed using Differential Scanning Calorimetry (DSC) and Thermogravimetric Analysis (TGA). DSC indicated an increase in the glass transition temperature (T_g) for the L3-5 formulation, suggesting enhanced rigidity and thermal stability.
- The coating's performance in the L3-5 formulation showed significant improvements, including enhanced hardness (2H), superior adhesion (5B ASTM rating), and better solvent resistance, compared to the unmodified ESO coating.
- The incorporation of lignin into ESO-based coatings significantly enhances corrosion resistance. The 3 wt.% lignin formulation (L3-5) exhibited a high impedance modulus higher than $10^8 \Omega \cdot \text{cm}^2$ after extended immersion in 3.5 wt.% NaCl solution, outperforming the neat ESO coating.
- The study indicates that lignin-reinforced ESO coatings represent a promising eco-friendly alternative to conventional epoxy coatings. They offer excellent corrosion protection while utilizing renewable materials, making them suitable for sustainable applications in industries requiring effective anti-corrosion coatings.

6. Limitations and Future Work

While the development of lignin-reinforced ESO coatings has yielded encouraging results in terms of corrosion resistance, there remain several areas for future research to enhance their mechanical and thermal properties.

A significant limitation is optimizing the physical mixing of lignin within the ESO matrix. The effectiveness of lignin as a reinforcing agent greatly depends on how well it is dispersed into the coating system. Future efforts should focus on achieving a more uniform dispersion of lignin throughout the matrix and experimenting with various types and concentrations of lignin. Variations in lignin's structure, including molecular weight and functional groups, could lead to better compatibility with the ESO and improve the overall effectiveness of the coatings. Although the cationic UV curing process utilized in this study has proven effective, modifying the curing parameters to accommodate higher lignin concentrations could further increase the mechanical and thermal properties of the coatings, without compromising corrosion resistance. This strategy would strike a crucial balance between optimal corrosion protection and enhanced strength under different environmental and mechanical stresses. Moreover, future investigations should consider the real-world performance of lignin-based coatings across diverse industrial settings. Assessments of long-term exposure, including tests under extreme conditions such as high humidity, fluctuating temperatures, and mechanical wear, are essential for validating the durability and effectiveness of these coatings over time.

In summary, future research should prioritize the optimization of lignin dispersion and the refinement of curing parameters to improve mechanical strength and performance under stress. Real-world evaluations and exploring the broader applicability of these coatings will be crucial for unlocking their full potential in industrial applications. These advancements could position lignin-based coatings as a sustainable and high-performance solution across various industries.

7. References

1. Wang, D. *et al.* Green synergy: Eco-friendly, high-performance anti-corrosion and wear-resistant coatings utilizing organosolv lignin and polydimethylsiloxane. *Prog Org Coat* **190**, 108365 (2024).
2. Dastpak, A. *et al.* From waste to valuable resource: lignin as a sustainable anti-corrosion coating. *Coatings* **8**, 454 (2018).
3. Auvergne, R., Caillol, S., David, G., Boutevin, B. & Pascault, J.-P. Biobased Thermosetting Epoxy: Present and Future. *Chem Rev* **114**, 1082–1115 (2014).
4. Noè, C. *et al.* New UV-curable anticorrosion coatings from vegetable oils. *Macromol Mater Eng* **306**, 2100029 (2021).
5. Chauhan, P., Chen, H., Roy Goswami, S. & Yan, N. Improved mechanical properties of flexible bio-based polymeric materials derived from epoxy mono/di-abietic acid and soyabean oil. *Ind Crops Prod* **138**, 111437 (2019).
6. Baroncini, E. A., Kumar Yadav, S., Palmese, G. R. & Stanzione III, J. F. Recent advances in bio-based epoxy resins and bio-based epoxy curing agents. *J Appl Polym Sci* **133**, (2016).
7. Malburet, S. *et al.* Sustainable access to fully biobased epoxidized vegetable oil thermoset materials prepared by thermal or UV-cationic processes. *RSC Adv* **10**, 41954–41966 (2020).
8. M. Shahbandeh. Soybean Oil Production Volume Worldwide. <https://www.statista.com/statistics/620477/soybean-oil-production-volume-worldwide/> (2025).
9. Ammar, S., Iling, A. W. M., Ramesh, K. & Ramesh, S. Development of fully organic coating system modified with epoxidized soybean oil with superior corrosion protection performance. *Prog Org Coat* **140**, 105523 (2020).
10. Teijido, R., Ruiz-Rubio, L., Lanceros-Méndez, S., Zhang, Q. & Vilas-Vilela, J. L. Sustainable bio-based epoxy resins with tunable thermal and mechanic properties and superior anti-corrosion performance. *Polymers (Basel)* **15**, 4180 (2023).
11. Ma, S., Jiang, Y., Liu, X. & Fan, L. Bio-based tetrafunctional crosslink agent from gallic acid and its enhanced soybean oil-based UV-cured coatings with high performance. *RSC Adv* **4**, 23036 (2014).

12. Ma, Q., Liu, X., Zhang, R., Zhu, J. & Jiang, Y. Synthesis and properties of full bio-based thermosetting resins from rosin acid and soybean oil: the role of rosin acid derivatives. *Green Chemistry* **15**, 1300–1310 (2013).
13. Jang, N. R., Kim, H., Hou, C. T. & Kim, B. S. Novel biobased photo-crosslinked polymer networks prepared from vegetable oil and 2, 5-furan diacrylate. *Polym Adv Technol* **24**, 814–818 (2013).
14. Barkane, A., Kampe, E., Platnieks, O. & Gaidukovs, S. Cellulose nanocrystals vs. cellulose nanofibers: A comparative study of reinforcing effects in uv-cured vegetable oil nanocomposites. *Nanomaterials* **11**, 1791 (2021).
15. Liu, Z., Erhan, S. Z., Akin, D. E. & Barton, F. E. “Green” composites from renewable resources: preparation of epoxidized soybean oil and flax fiber composites. *J Agric Food Chem* **54**, 2134–2137 (2006).
16. Zhou, S. *et al.* Rigid-and-Flexible, Degradable, Fully Biobased Thermosets from Lignin and Soybean Oil: Synthesis and Properties. *ACS Sustain Chem Eng* **11**, 3466–3473 (2023).
17. Zhen, X. *et al.* Fully bio-based epoxy resins from lignin and epoxidized soybean oil: Rigid-flexible, tunable properties and high lignin content. *Int J Biol Macromol* **254**, 127760 (2024).
18. Komartin, R. S., Balanuca, B., Necolau, M. I., Cojocaru, A. & Stan, R. Composite materials from renewable resources as sustainable corrosion protection coatings. *Polymers (Basel)* **13**, 3792 (2021).
19. Sun, R. Lignin Source and Structural Characterization. *ChemSusChem* **13**, (2020).
20. Fodil Cherif, M., Trache, D., Brosse, N., Benaliouche, F. & Tarchoun, A. F. Comparison of the Physicochemical Properties and Thermal Stability of Organosolv and Kraft Lignins from Hardwood and Softwood Biomass for Their Potential Valorization. *Waste Biomass Valorization* **11**, 6541–6553 (2020).
21. Constant, S. *et al.* New insights into the structure and composition of technical lignins: a comparative characterisation study. *Green Chemistry* **18**, 2651–2665 (2016).
22. Wu, M., Cui, B., Liu, H. & Wang, Z. A lignin/castor oil-based polyamide autonomous self-healing composite materials. *Int J Biol Macromol* **305**, 141159 (2025).

23. Wang, D. *et al.* Recent findings on lignin-based wear and corrosion resistance coatings. *Corrosion Reviews* (2024).
24. Wang, J., Seidi, F., Huang, Y. & Xiao, H. Smart lignin-based polyurethane conjugated with corrosion inhibitor as bio-based anticorrosive sublayer coating. *Ind Crops Prod* **188**, 115719 (2022).
25. Wang, J. *et al.* Lignin self-healing coatings based on thermo-reversible Diels-Alder reaction for anticorrosion applications. *Prog Org Coat* **191**, 108428 (2024).
26. Komartin, R. S., Balanuca, B., Necolau, M. I., Cojocaru, A. & Stan, R. Composite materials from renewable resources as sustainable corrosion protection coatings. *Polymers (Basel)* **13**, 3792 (2021).
27. Abliz, Dilmurat *et al.* Curing Methods for Advanced Polymer Composites - A Review. *Polymers and Polymer Composites* **21**, 341–348 (2013).
28. Abliz, D. *et al.* Curing methods for advanced polymer composites-a review. *Polymers and Polymer Composites* **21**, 341–348 (2013).
29. Tan, S. G. & Chow, W. S. Curing Characteristics and Thermal Properties of Epoxidized Soybean Oil Based Thermosetting Resin. *Journal of Oil & Fat Industries* **88**, 915–923 (2010).
30. Sangermano, M., Razza, N. & Crivello, J. V. Cationic UV-curing: Technology and applications. *Macromol Mater Eng* **299**, 775–793 (2014).
31. Pierau, L. *et al.* Bio-sourced monomers and cationic photopolymerization–The green combination towards eco-friendly and non-toxic materials. *Prog Polym Sci* **127**, 101517 (2022).
32. Noè, C., Hakkarainen, M. & Sangermano, M. Cationic UV-curing of epoxidized biobased resins. *Polymers (Basel)* **13**, 89 (2020).
33. Noè, C. *et al.* Cationic photopolymerization of bio-renewable epoxidized monomers. *Prog Org Coat* **133**, 131–138 (2019).
34. Han, T. L., Kumar, R. N., Rozman, H. D. & Noor, M. A. M. GMA grafted sago starch as a reactive component in ultra violet radiation curable coatings. *Carbohydr Polym* **54**, 509–516 (2003).

35. Wan Rosli, W. D., Kumar, R. N., Mek Zah, S. & Hilmi, M. M. UV radiation curing of epoxidized palm oil–cycloaliphatic diepoxide system induced by cationic photoinitiators for surface coatings. *Eur Polym J* **39**, 593–600 (2003).
36. Pezzana, L. *et al.* Cationic UV-curing of isosorbide-based epoxy coating reinforced with macadamia nut shell powder. *Prog Org Coat* **185**, 107949 (2023).
37. Noè, C., Iannucci, L., Malburet, S., Graillot, A. & Grassini, S. Vanillin-Based Photocurable Anticorrosion Coatings Reinforced with Nanoclays. *Macromol Mater Eng* **309**, 2400155 (2024).
38. Smith, B. C. *Fundamentals of Fourier Transform Infrared Spectroscopy*. (CRC press, 2011).
39. Henn, K. A., Forsman, N., Zou, T. & Österberg, M. Colloidal Lignin Particles and Epoxies for Bio-Based, Durable, and Multiresistant Nanostructured Coatings. *ACS Appl Mater Interfaces* **13**, 34793–34806 (2021).
40. Notley, S. M. & Norgren, M. Surface Energy and Wettability of Spin-Coated Thin Films of Lignin Isolated from Wood. *Langmuir* **26**, 5484–5490 (2010).
41. Cristoforetti, A., Rossi, S., Deflorian, F. & Fedel, M. On the limits of the EIS low-frequency impedance modulus as a tool to describe the protection properties of organic coatings exposed to accelerated aging tests. *Coatings* **13**, 598 (2023).

Acknowledgments

I am profoundly grateful to my supervisor, Professor Messori, for his continuous support and for providing me with the opportunity to take part in this research project. I also wish to extend my sincere appreciation to my co-supervisors, Dr. Noé and Dr. Iannucci, for their expert guidance, insightful advice, and steady encouragement throughout this work.

I am deeply thankful to my parents, Fariba and Masoud, my dear brother Hessam, as well as to our beloved cat Fandogh, whose love and support have been my greatest source of strength. I also want to thank Parisa, who has always felt like a sister to me, and even from afar, her presence fills me with motivation and gratitude.

I feel incredibly fortunate to have shared this journey with Maryam, Mahsa, Azade, and Pardis, friends who have stood by me through every challenge over the past decade. Your companionship means the world to me.

Lastly, I want to thank Fahime, Mahtab, and all my other friends who, in various ways, supported me in completing this thesis. Your kindness and help will always be remembered.